

Supplementary Information

Carbide-mediated catalytic hydrogenolysis: defects in graphene on carbonaceous lithium host for liquid and all-solid-state lithium metal batteries

Namhyung Kim^{a,d}, Hyungyeon Cha^{a,f}, Sujong Chae^b, Taeyong Lee^a, Yoonkwang Lee^c, Yujin Kim^a, Jaekyung
Sung^{*,a,e}, Jaephil Cho^{*,a}

^aDepartment of Energy Engineering, School of Energy and Chemical Engineering, Ulsan National Institute of Science and Technology (UNIST), 50, UNIST-gil, Ulsan 44919, Republic of Korea

^bDepartment of Industrial Chemistry, Pukyong National University, Busan 48513, Republic of Korea

^cAdvanced Battery Development Team, Hyundai Motor Company, Hwaseong, 18280 Republic of Korea

^dPresent address: Energy & Environment Directorate, Pacific Northwest National Laboratory (PNNL), 902 Battelle Boulevard, Richland, Washington 99354, United States

^ePresent address: Department of Nuclear Science and Engineering, Massachusetts Institute of Technology (MIT), Cambridge, MA, United States

^fPresent address: Energy Storage and Distributed Resources Division, Lawrence Berkeley National Laboratory (LBNL), Berkeley, California 94720, United States

*Corresponding author: jpcho@unist.ac.kr

Experimental section

Preparation of the GR|CM-hy-C

Commercially available carbon cloth (Toray Industries, Inc.) was used for a substrate material. The carbon cloth (4 cm × 5 cm) was rinsed with isopropanol and deionized water. Transition metal (TM) hydroxides were coated on the carbon cloth by simple chemical bath deposition method. For Fe hydroxide coated CC, solution was prepared by mixing 200 mL of deionized water, 0.06 M $\text{Fe}(\text{NO}_3)_3 \cdot 9\text{H}_2\text{O}$ (Sigma Aldrich, $\geq 98\%$), and 0.3 M urea (Sigma Aldrich, 99.0%) in a 500 mL beaker at room temperature. In case of Ni hydroxide coated CC, 0.06 M $\text{Ni}(\text{NO}_3)_2 \cdot 6\text{H}_2\text{O}$ (Sigma Aldrich, $\geq 97.0\%$) was used instead of Fe nitrate nonahydrate. The rinsed carbon cloth was immersed into the beaker containing the prepared solution. Then, the beaker was sealed by an aluminum foil and heated up to 90°C for 2 h in a convection drying oven. After the solution naturally cooled down to room temperature, the carbon cloth was rinsed with deionized water several times using ultrasonic and dried at 80°C over 4 h under a vacuum to remove residual water content in TM hydroxide coated CC. The weight changes of each sample were presented in Table S5.

To reduce the TM hydroxides into TM metals and trigger the catalytic hydrogenolysis, the as-obtained TM hydroxide coated CCs were placed in a tube furnace and annealed under Ar/H_2 (90/10 volume ratio) atmosphere with a flow rate of 0.8 L min^{-1} . In this process, two annealing conditions were successively applied for the hydroxide reduction (500°C for 30 min) and the catalytic hydrogenolysis (950°C for 45 min), respectively. After the TM catalytic hydrogenolysis, the samples were naturally cooled down to room temperature, and the CM-hy-C and hy-C were finally obtained with a reduced weight by carbon gasification (Table S6).

For the galvanic replacement reaction of each sample, 50 mL of $10\ \mu\text{M}$ $\text{HAuCl}_4 \cdot 3\text{H}_2\text{O}$ (Sigma Aldrich, $\geq 99.9\%$) solution was prepared in a 100 mL vial with 20 mL of deionized water, and the CM-hy-C and hy-C were placed into the solution, respectively. Then, the vials containing the solution and hydrogenated carbon cloth was stirred lightly for 1 hour. After the galvanic displacement, the obtained GR|CM-hy-C and GR|hy-C were washed by isopropanol and deionized water several times and dried over 4 h at 60°C under a vacuum. Even if all Au ions in the solution are replaced and deposited on the substrate, the content of Au in GR|CM-hy-C is only below 0.05 wt%. The weight change of each sample after the galvanic replacement were plotted in Table S7.

The galvanic replaced; Fe particle coated carbon cloth was prepared as a control sample which has no catalytic hydrogenolysis reaction during sample preparation steps. The Fe hydroxide coated carbon cloth was prepared by same method described above. Then, it was placed in a tube furnace and annealed at 500°C for 30 min under Ar/H_2 (90/10 volume ratio) atmosphere with a flow rate of 0.8 L min^{-1} , to reduce the Fe hydroxide into Fe metal. The Fe coated carbon was placed into 50 mL of $10\ \mu\text{M}$ $\text{HAuCl}_4 \cdot 3\text{H}_2\text{O}$ solution for the galvanic displacement reaction. After 1 hour of stirring, the obtained GR|C was washed by isopropanol and deionized water several times and dried over 4 h at 60°C under a vacuum.

Material characterization

Structural characterization of the samples was conducted using scanning electron microscopy (SEM, VERIOS 460, FEI) and high-resolution transmission electron microscopy (HR-TEM, ARM300, JEOL). For the TEM analysis, the samples were prepared by dual-beam focused ion beam milling (Helios 450HP, FEI) with a 2-30 kV Ga ion beam. Before the focused ion beam treatment, Ga deposition was applied on the surface of each sample to avoid damage from the Ga ion beam. For the cross-sectional SEM analysis, the ion milling system (IM-4000, Hitachi) was performed to cut and polish the cross-section of each sample. In case of cycled or lithiated samples, a preparation of their cross-section was done by cutting them with a razor blade. The surface chemistry and chemical states of the sample was analyzed by X-ray photoelectron spectroscopy (K-alpha spectrometer, Thermo Scientific) with a depth profiling method. Raman spectroscopy (NRS-5000, Jasco) was performed to characterize the carbon structure of samples. The structural analysis was performed using an X-ray diffractometer (D/Max2000, Rigaku). For the post-cycling characterization, the cycled pouch or coin type cells were disassembled, and rinsed by dimethyl carbonate several times in an Ar-filled glovebox (Korea Kiyon, O₂ < 0.1 ppm, H₂O < 0.1 ppm). Then, the as-prepared samples were sealed in an Ar-filled bag and immediately transferred to the characterization instruments.

Electrochemical characterization for LIB

The electrochemical performances of each sample with a metallic lithium counter electrode were evaluated with a galvanostatic cycling of coin-type cells (CR2032, Hohsen corp.). The full-cell performances with NCM811 cathode were evaluated in a pouch-type cells. A 12 μm thick polyethylene (W-Scope) was used as a separator for all the cell tests including coin-type and pouch-type cells. The electrolyte formulation for the nucleation overpotential and Li plating/stripping test (Fig.4a) was 1.0 M lithium bis(trifluoromethanesulfonyl)imide (LiTFSI, Panax Etec) in 1,3-dioxolane (DOL):1,2-dimethoxyethane (DME) by 1:1 volume ratio.

For both the Li plating/fully delithiation test (Fig.4b) and pouch-type cells, the electrolyte formulation was 0.6 M LiTFSI, 0.4 M lithium bis-(oxalate)borate (LiBOB, Sigma Aldrich), and 0.05 M lithium hexafluorophosphate (LiPF₆, Panax Etec) in ethylene carbonate (EC, Soulbrain):ethyl methyl carbonate (EMC, Soulbrain) by 2:1 volume ratio with 1 wt% fluoroethylene carbonate (FEC, Soulbrain), 2 wt% vinylene carbonate (VC, Soulbrain), 0.5 wt% lithium nitrate (LiNO₃, Soulbrain), and 0.5 wt% lithium tetrafluoroborate (LiBF₄, Soulbrain). For the full-cell test in conventional LiPF₆-based carbonate electrolyte, the electrolyte formulation was 1.3 M LiPF₆ in EC:EMC:DEC by 3:5:2 volume ratio with 5 wt% FEC, 0.2 wt% VC, and 0.2 wt% LiBF₄.

For the nucleation overpotential and Li plating/stripping analysis, each of Cu foil, pristine CC, CM-hy-C, hy-C, GR|CM-hy-C, and GR|hy-C (16 mm in diameter) were used as the working electrode, and 500 μm thick Lithium foil (Honjo Metal, > 99%) was used as the counter electrode. Before the Li plating/stripping test (Fig.4a), 2 mAh cm⁻² of lithium was deposited on each sample with a C-rate of 0.1C. The Li nucleation overpotential and Li plating/stripping test was conducted by a battery cyler (TOSCAT-3100, Toyo system) in an isothermal chamber (25 ° C).

For the pouch-type full-cell evaluation, cathode electrode of over 3.2 mAh cm⁻² LiNi_{0.8}Co_{0.1}Mn_{0.1}O₂ (single crystalline NCM811, homemade) was fabricated by spreading a slurry composed of 95 wt% NCM811, 2 wt% carbon black (Super C65, Imerys Graphite & Carbon), 1 wt% graphite (SFG6L, Imerys Graphite & Carbon), and 2 wt% poly(vinylidene fluoride) (Solef6020, Solvay) in 1-methyl-2-pyrrolidinone (Sigma Aldrich) on aluminum foil (15 μm). Areal mass loading of the cathode was over 16.7 mg cm⁻². The cathode electrode was calendered up to 3.3 g cm⁻³ of electrode density by a roll pressing machine and dried at 120 ° C for 10 hours under vacuum. Each electrode was cut to 2.8 cm × 2.8 cm (cathode) and 3 cm × 3 cm (anode). The pouch-type full-cell was fabricated in a dry room (relative humidity, 0.05%; 20 ° C) by conventional pouch cell assembly methods (ultrasonic welding and vacuum sealing with electrolyte injection). The amount of electrolyte per capacity was 20 μl mAh⁻¹.

The pouch-type full-cell cycling was carried out within the voltage window of 4.3 V and 3.0 V at 25 ° C (charge: 0.25 C, 0.75 mA cm⁻², discharge: 0.5 C, 1.5 mA cm⁻²) by the TOSCAT-3100 cycler. Li-free tests were conducted in coin-type cell after precycling of anode for 1 cycle. For the pre-stored Li, pouch-type cells of each sample were fabricated with Li metal foil, and the Li was electrochemically deposited (2.0 mAh cm⁻²) on each sample. Then, the pouch cell was disassembled and re-assembled with cathode electrode for full-cell tests. For 3-electrode full-cell evaluation, the additional lithium piece was introduced into the pouch-type full-cell as a reference electrode. The 3-electrode analysis was conducted within the voltage window of 4.3V to 2.8 V at 25 ° C (charge/discharge: 0.3 C, 0.9 mA cm⁻²) by a single channel cycler (Wonatech).

For high temperature cycling test, the pouch-type full-cells were placed at an isothermal chamber with ambient temperature (60 °C). The cycling condition was same with those of testing protocols for room temperature cycling.

For a DCIR measurement, pouch-type full-cell using each anode was carried out. After finishing the 1st charge and discharge process with 0.1 C-rate, the cells were charged up to 50% of state of charge (SOC) under 0.2 C-rate. Then, the series of discharge and charge process were applied for 10 seconds with 0.5, 1.0, 1.5, 2.0, and 2.5 C-rate, respectively. Voltage difference before and after applying the current pulse, derived from ohmic resistance, were used to calculate the cell resistance as applied current densities.

In-situ dilatometry

In-situ thickness change of the pouch-type cells with NCM811 cathode for each sample was measured by customized dilatometry system (Mitutoyo) with a battery cycler (WBCS-3000, Wonatech). The small constant pressure of 2.23 kPa was applied on the pouch cell by weights to avoid electrode floating. The dilatometry was carried out within the voltage window of 4.3 V and 3.0 V at the room temperature by the WBCS-3000 cycler. In this dilatometry evaluation, we assumed that NCM811 just acts as a lithium source and will not contribute any electrode thickness change because the volume change of layered cathode is normally negligible compared to those of lithium metal anode. For the precise measurement of thickness change, all test was performed on the precision granite surface plate.

Electrode and cell preparation for ASSB

Commercial Li₆PS₅Cl (NEI Corporation, United states) was used for the solid-state electrolyte separator layer. 90 mg power-typed Li₆PS₅Cl was loaded in a pressurized cell with a diameter of 1 cm and then was calendered with the pressure of 200 MPa to make it pellet-shaped. Homemade niobium coated single crystalline NCM811, Li₆PS₅Cl, and Super C65 were first mixed in a mortar and pestle in a weight ratio 67:30:3, respectively and prepared mixed powder (30.4 mg cm⁻²) was put in cathode side of the cell. The GR|CM-hy-C was grinded in mortar and prepared powder (1.2 mg cm⁻²) was used for the anode electrode film which contains 95 wt% of GR|CM-hy-C and 5 wt% of carboxymethyl cellulose (Nippon paper). Subsequently, the cathode mixture, solid-state electrolyte separator layer, and prepared GR|CM-hy-C film were stacked together and pressed at 700 MPa and then Li foil (50 μm) were added to the bottom of the anode side. As sulfide-based materials and Li are sensitive to air and moisture, all these procedures were done within an Argon-filled glovebox (Korea Kiyon, H₂O < 0.1 ppm, O₂ < 0.1 ppm).

Electrochemical characterization for ASSB

At the first cycle in a full-cell configuration, 0.41 mA cm⁻² of current density was applied, and the operating voltage range was between 4.3 V and 2.5 V. At the rest of cycles, 1.25 mA cm⁻² of current density was applied, and the voltage range was between 4.3 V and 2.7 V. All cells were evaluated in isothermal chamber (60 ° C) with the stack pressure of 60 MPa.

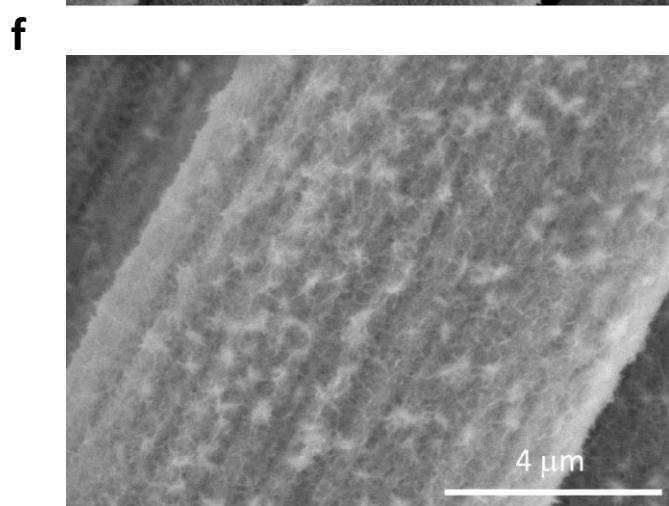
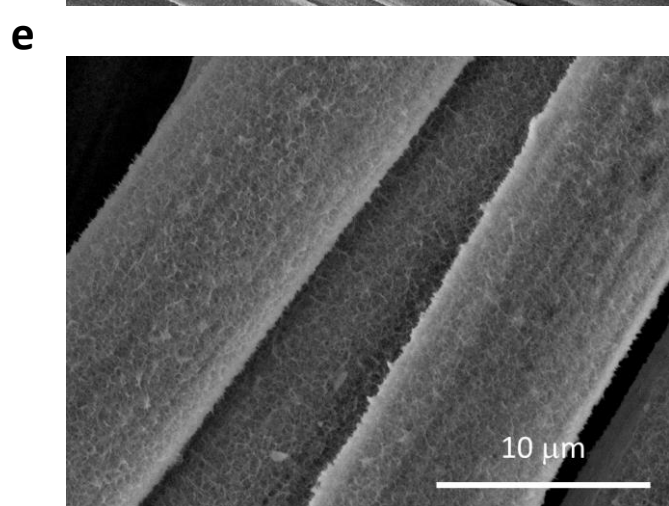
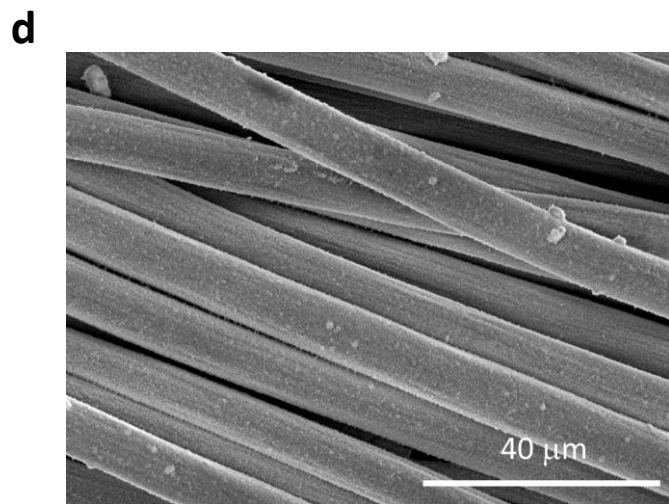
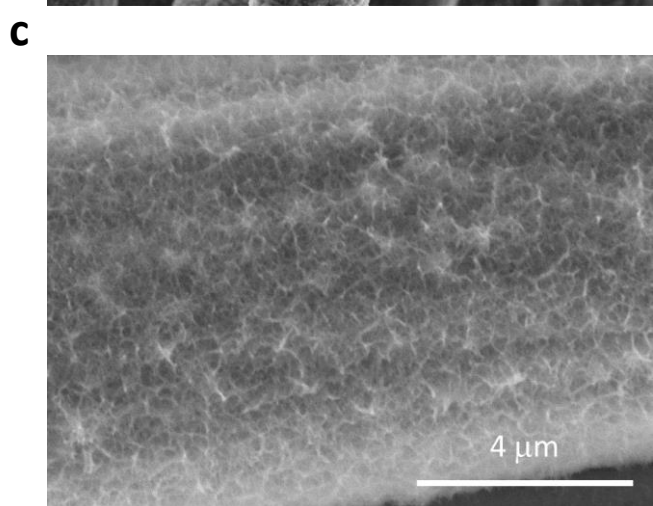
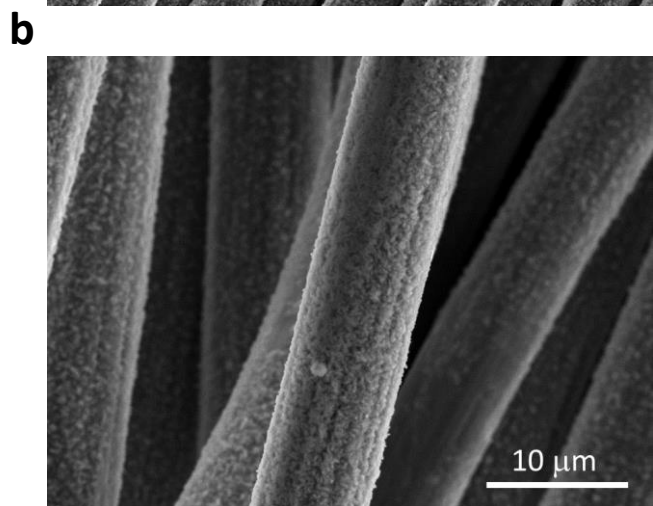
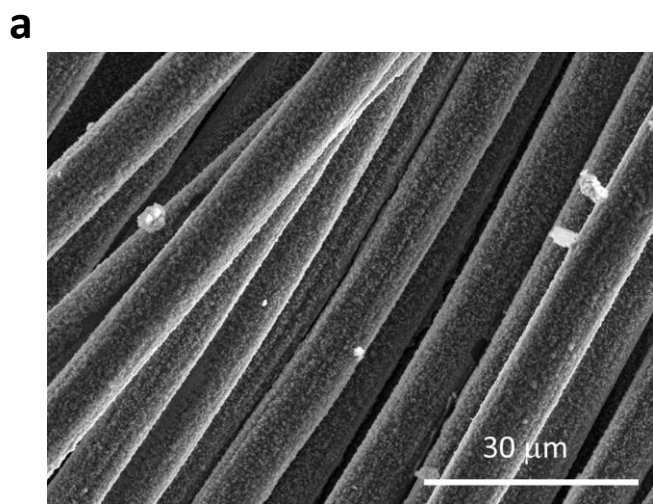


Fig.S1. a-c, SEM images of Ni hydroxide coated carbon cloth. d-f, SEM images of Fe hydroxide coated carbon cloth.

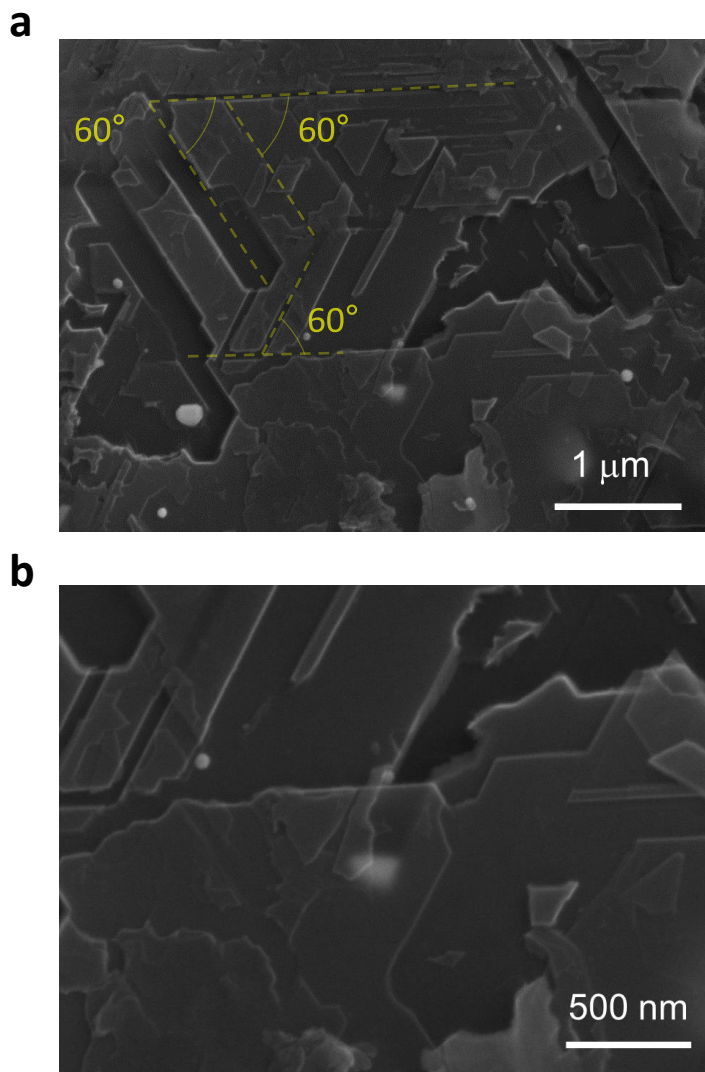


Fig.S2. a, SEM image of commercial graphite after the catalytic hydrogenolysis reaction. b, magnified SEM image of Ni catalyst for the catalytic hydrogenolysis. In case of the graphite having high crystallinity, the catalytic hydrogenolysis anisotropically occur parallel to the $\langle 11\bar{2}0 \rangle$ directions.

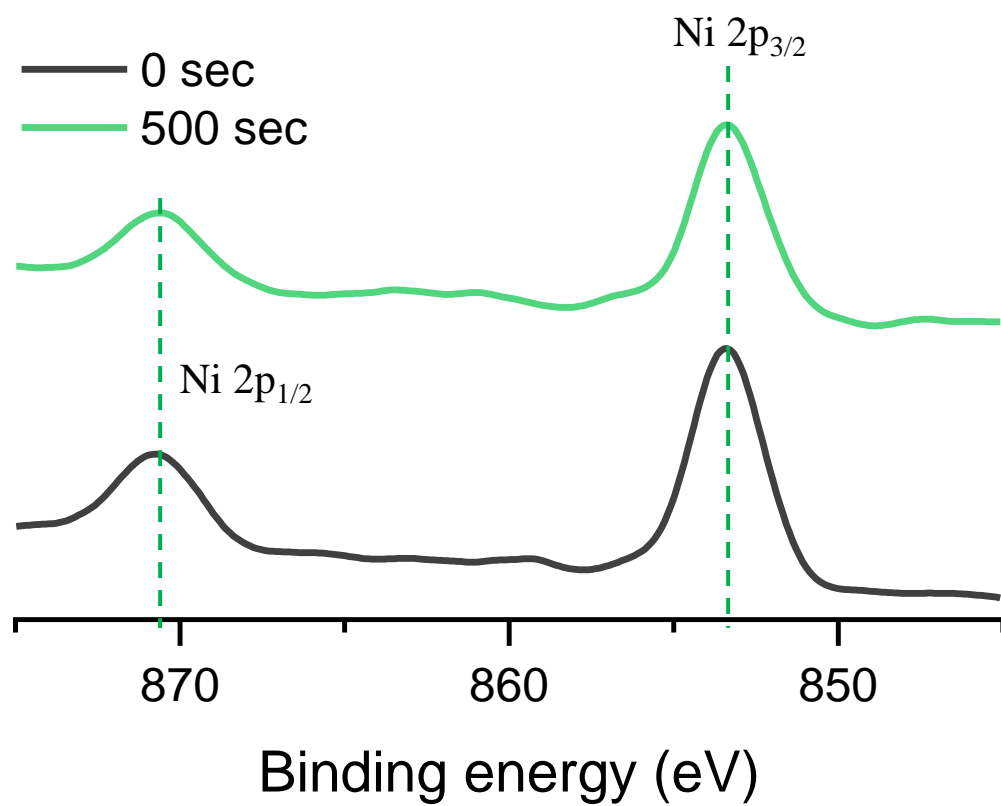


Fig.S3. XPS depth profiling analysis of hy-C. The hy-C had similar XPS profiles between surface and sub-surface without any Ni-C characteristic peak because of unstable Ni-C phase.

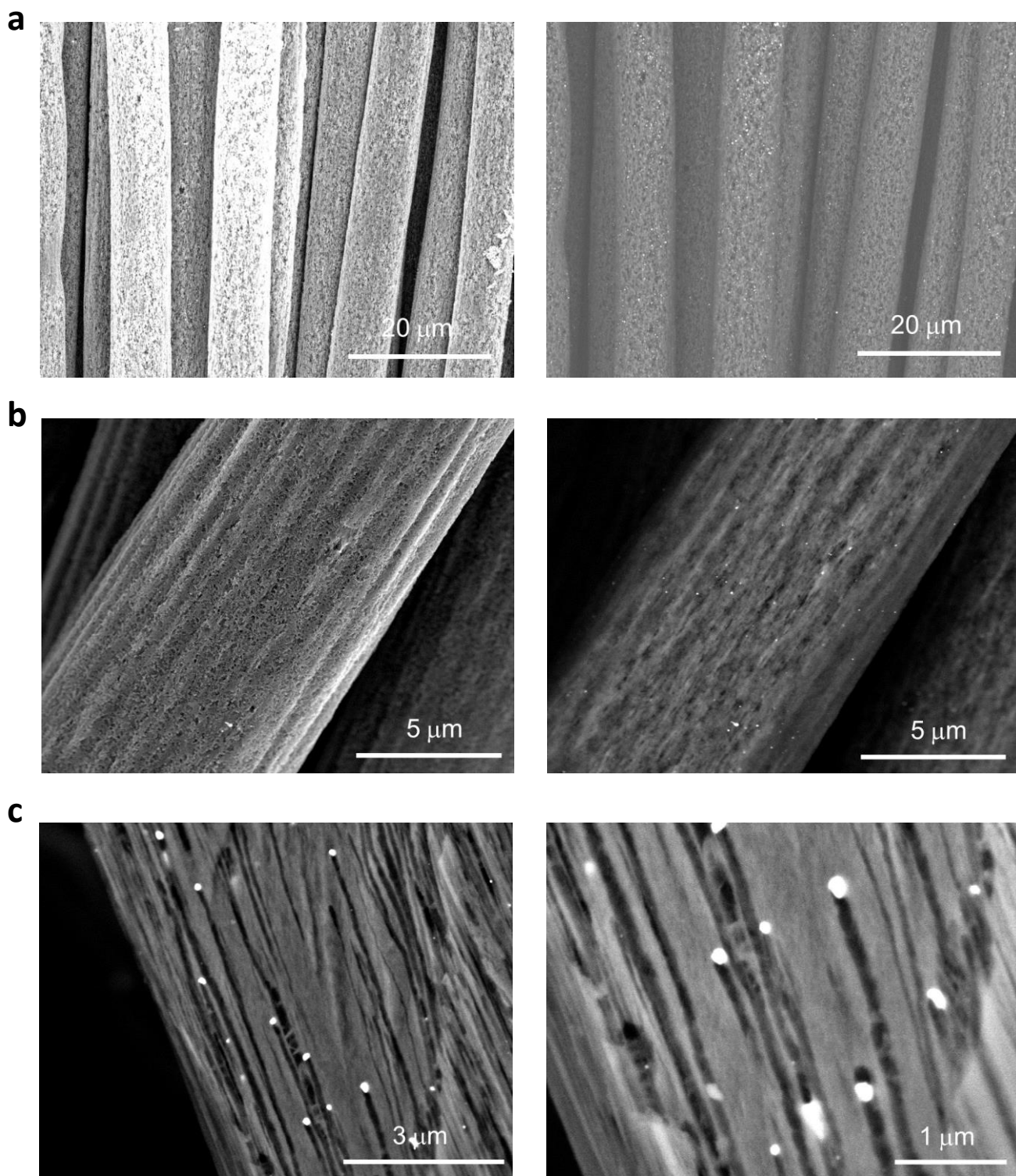


Fig.S4. a-c, SEM (left) and back-scattered electron SEM (right) images of hy-C in various magnification. Carbon substrate was etched, and porous nano-channels were produced by Ni catalysts during the catalytic hydrogenolysis (c).

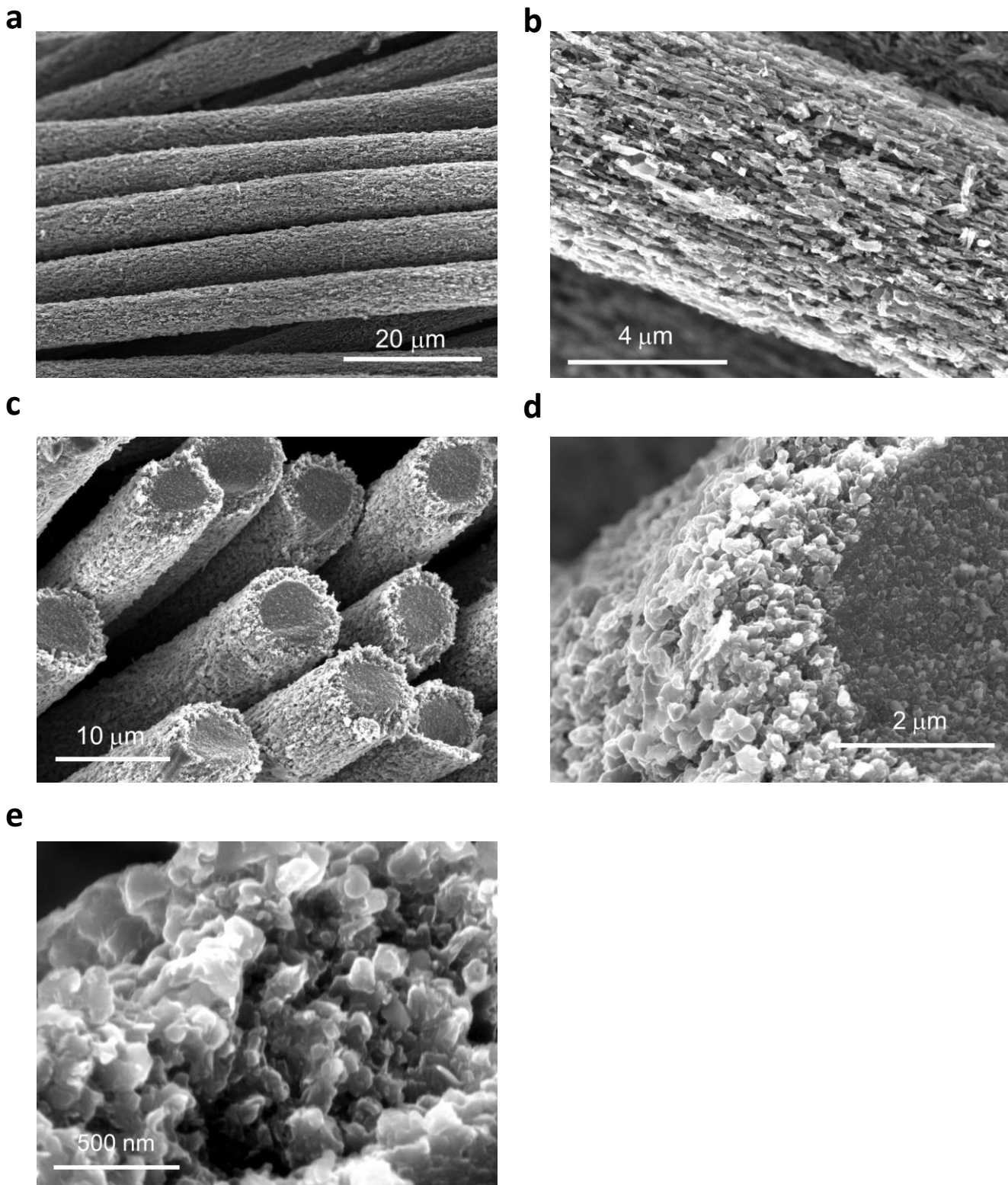
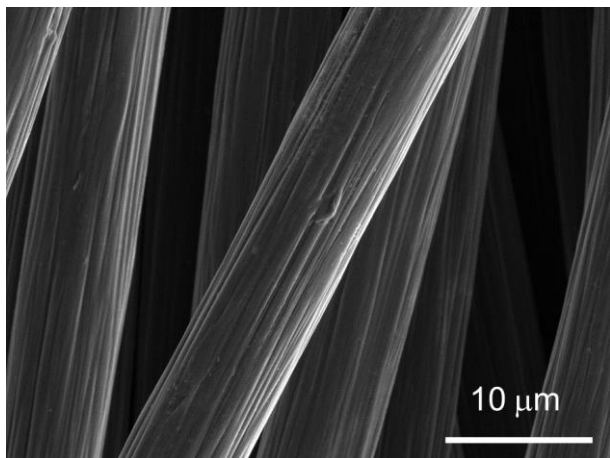


Fig.S5. **a,b**, SEM images of CM-hy-C. **c,d**, SEM images of cross-sectional CM-hy-C. The sample was cut by razor blade. **e**, SEM image of the surface of CM-hy-C indicating Fe-catalyzed layer with numerous graphitic shells and nano-channels.

a



b

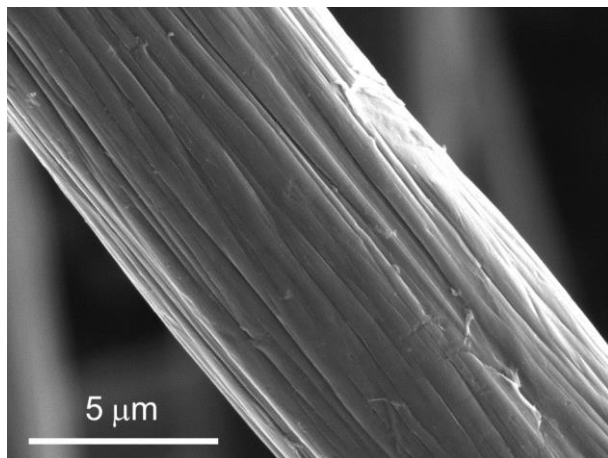


Fig.S6. a,b, SEM images of pristine carbon cloth.

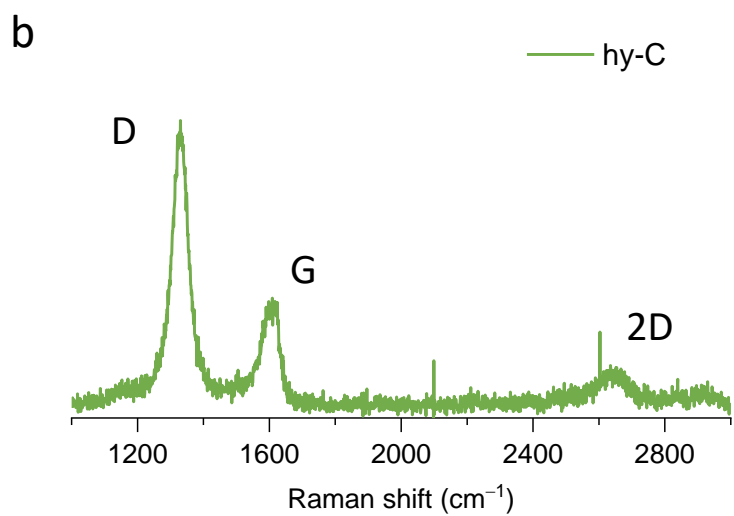
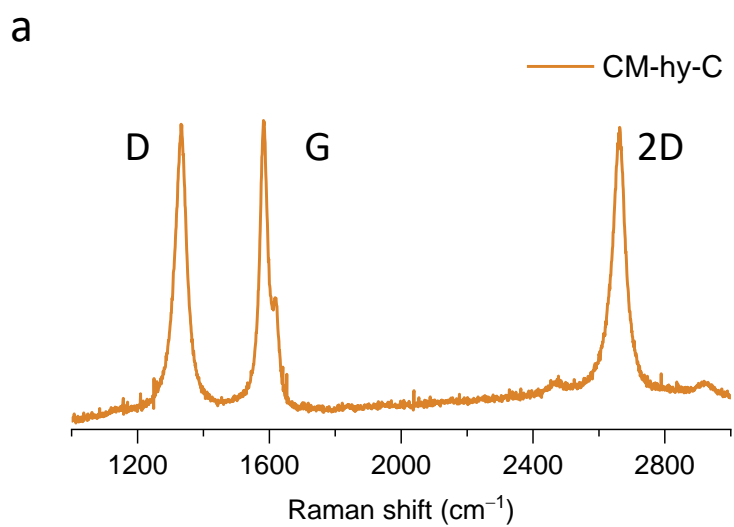


Fig.S7. a,b, Raman spectroscopy of CM-hy-C (a) and hy-C (b).

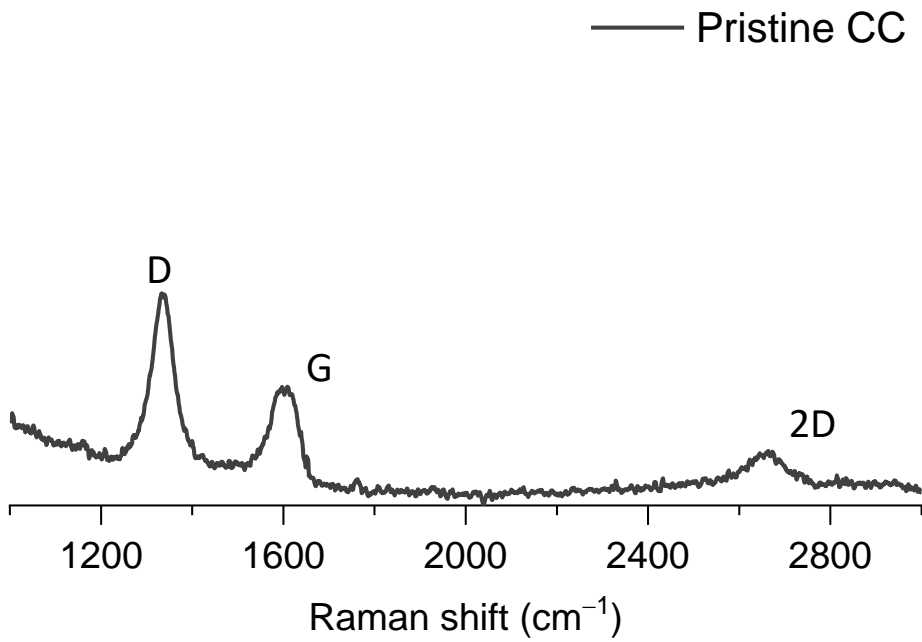


Fig.S8. Raman spectroscopy of pristine carbon cloth.

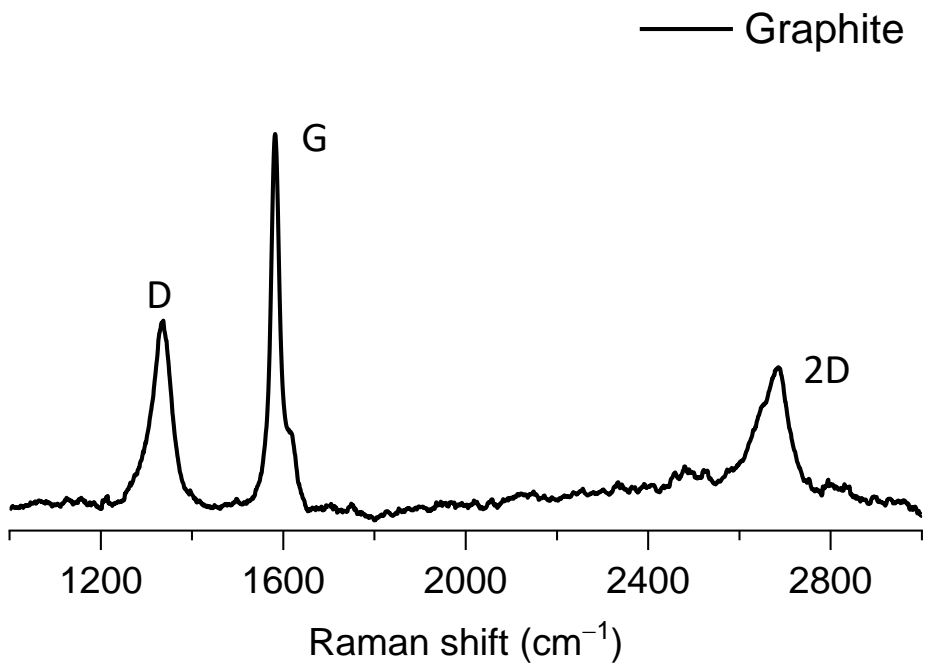


Fig.S9. Raman spectroscopy of commercial graphite.

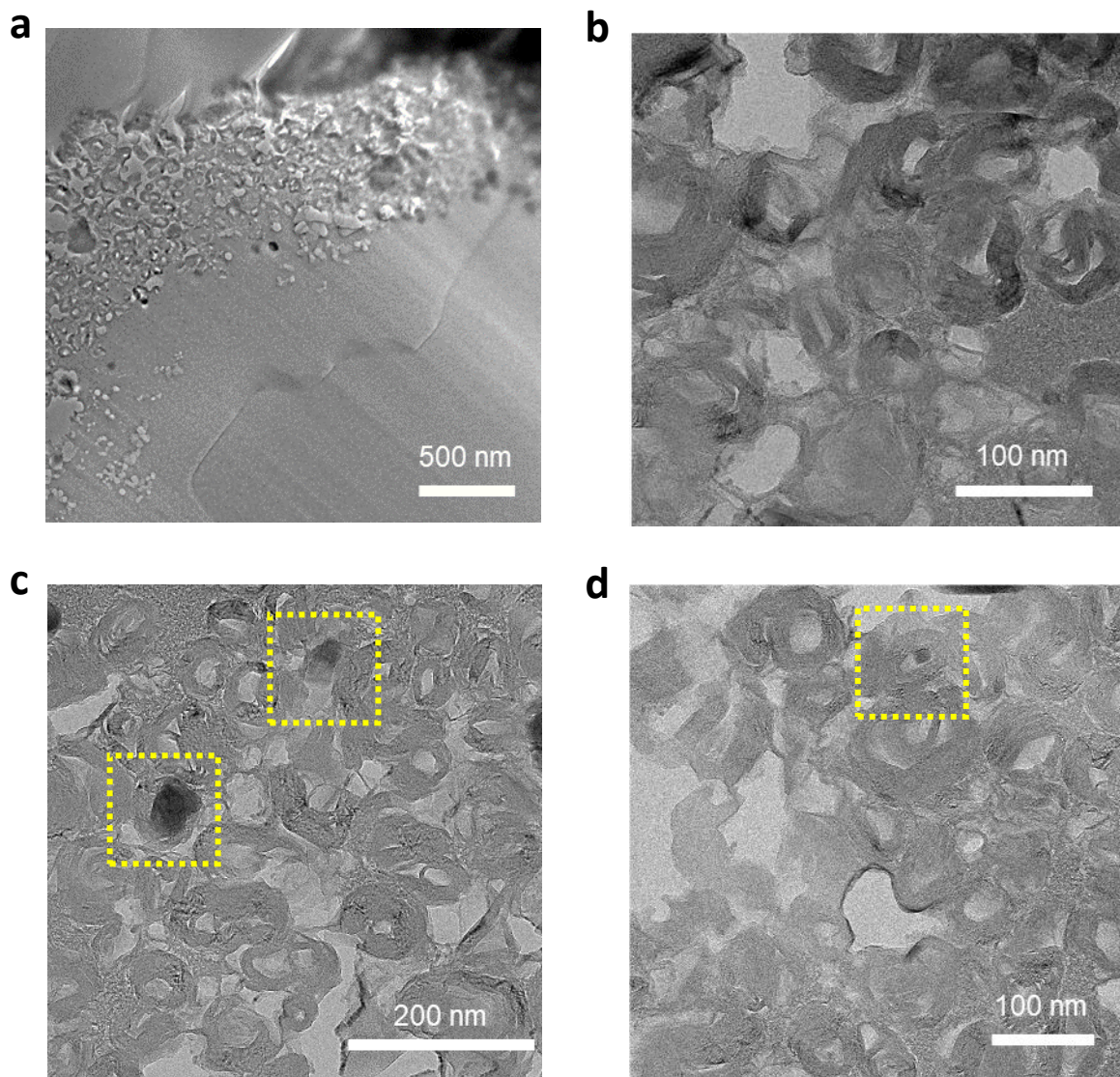


Fig.S10. TEM images of cross-sectional CM-hy-C. The cross-sectional sample was prepared by FIB treatment. **a**, low magnification image. **b-d**, TEM images of graphitic shell on the surface of CM-hy-C. The dot-lined yellow boxes (c and d) indicate Fe catalysts placed in the graphitic shell and nano-channel.

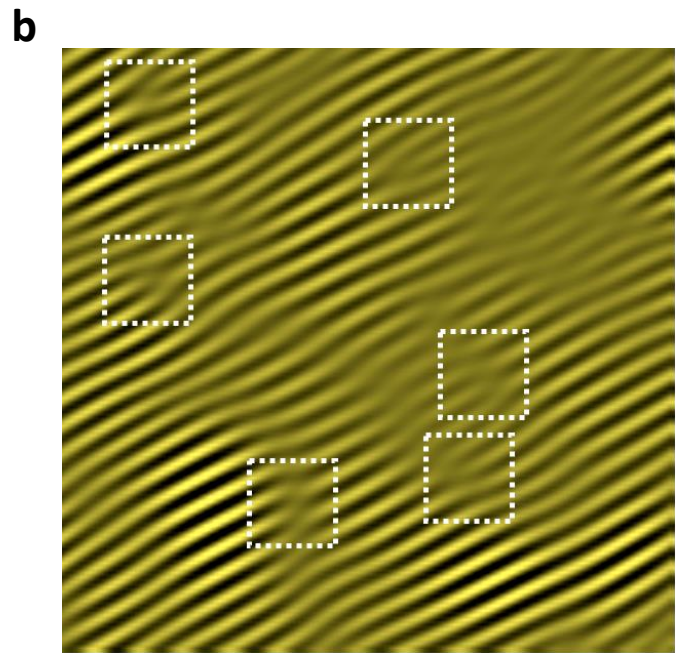
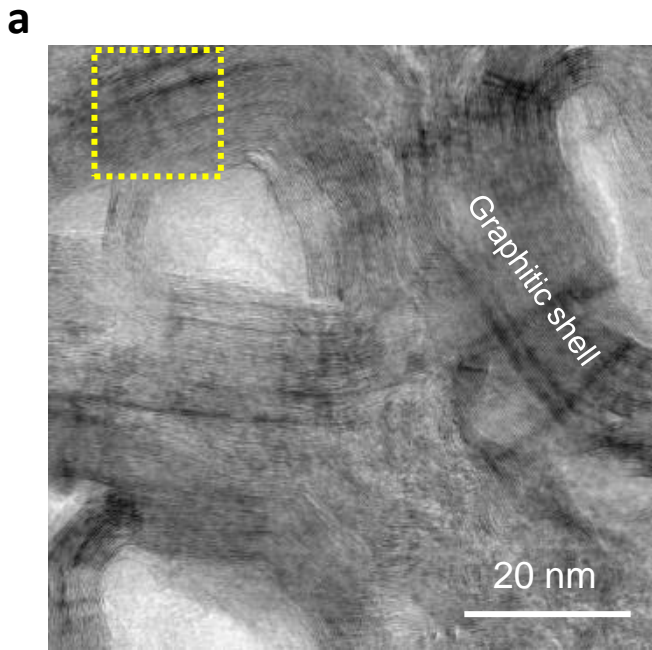


Fig.S11. **a**, High-resolution TEM image from Fig.2f. **b**, inversed FFT image of yellow boxed area in (a) to investigate the defective structure of graphitic shell.

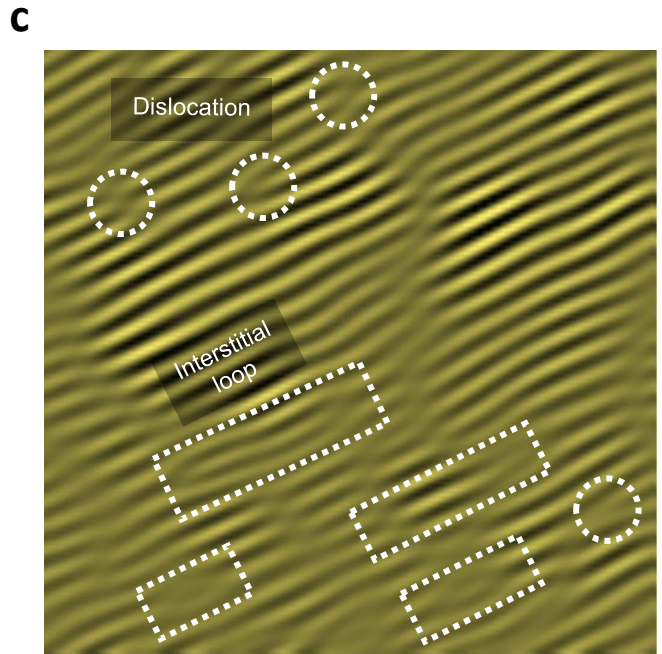
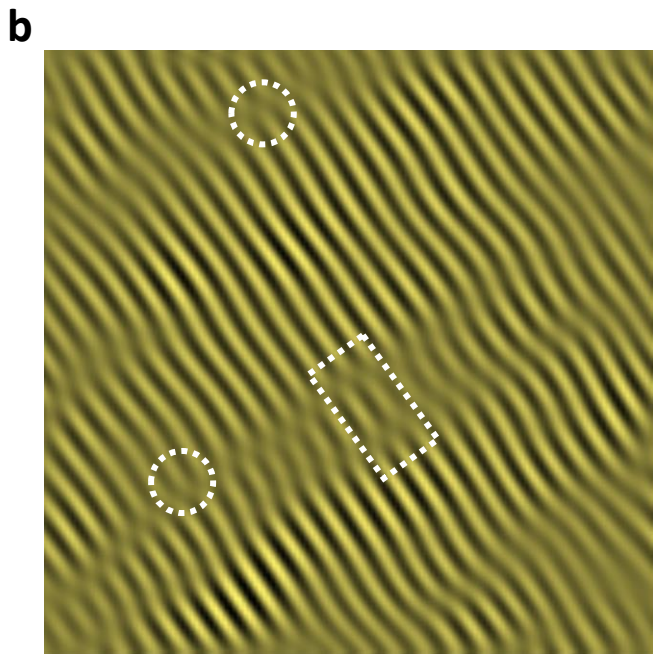
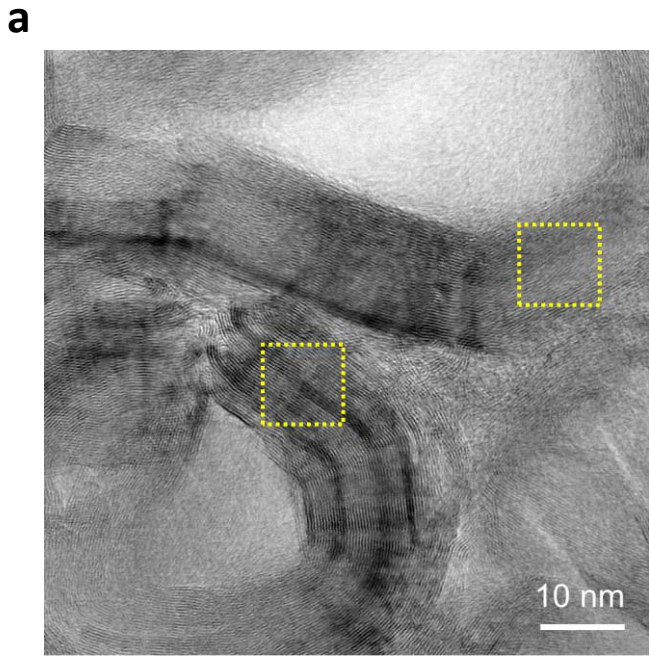


Fig.S12. **a**, High-resolution TEM image of graphitic shell in CM-hy-C. **b,c**, inversed FFT images from the dot-lined boxes of (a) to investigate the defective structure of graphitic shell.

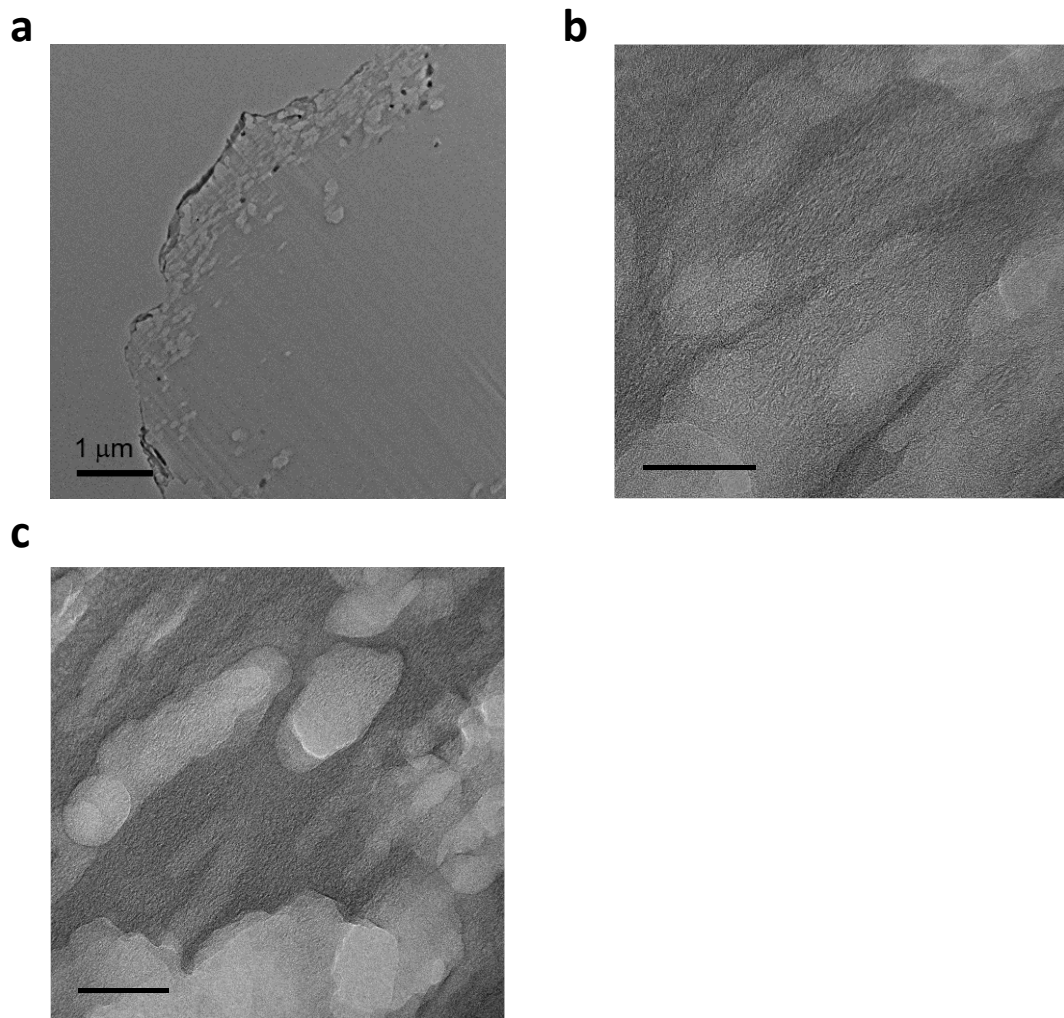


Fig.S13. TEM images of cross-sectional hy-C. The cross-sectional sample was prepared by FIB treatment. **a**, low magnification image. **b-c**, TEM images of nano-channels on the surface of hy-C.

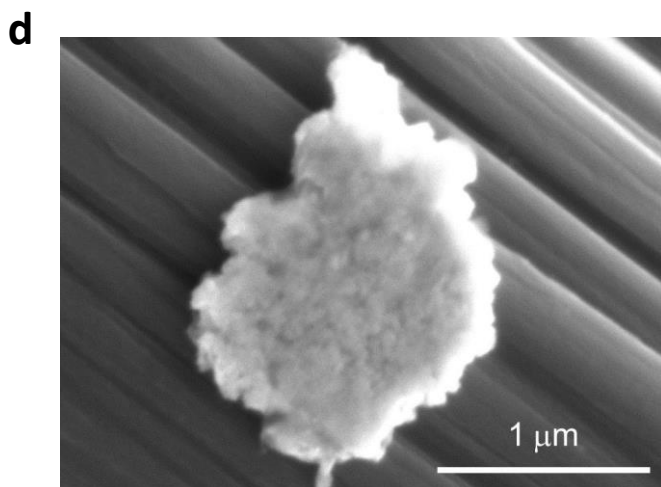
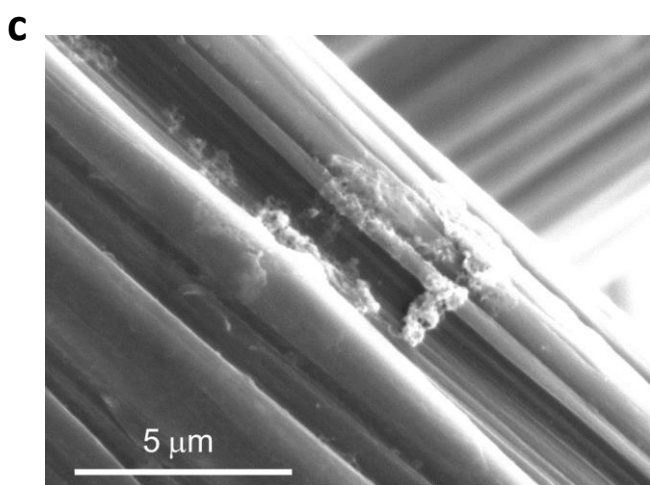
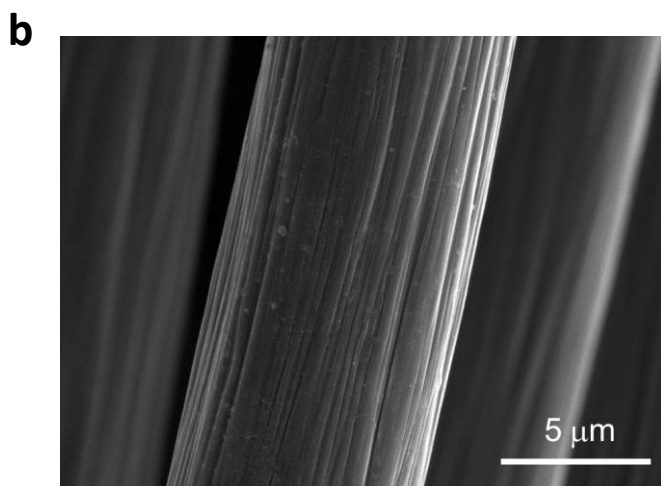
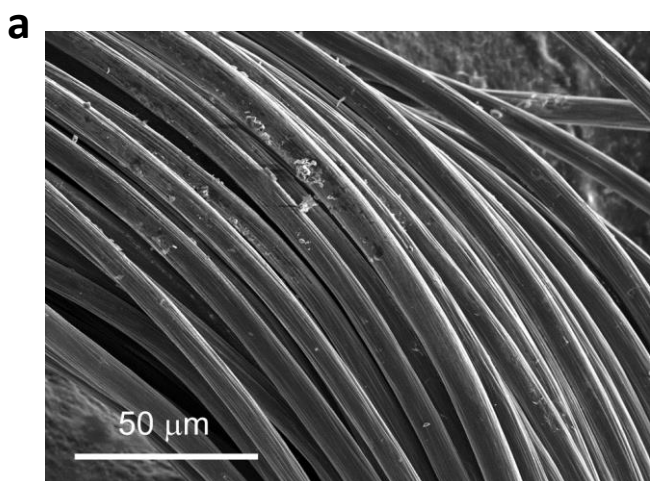


Fig.S14. SEM images of pristine carbon cloth after galvanic replacement reaction. There was no Au displacement on the surface of pristine carbon cloth because of absence of electron donor sacrificial metal species. Trace of residual HAuCl₄ was observed (c and d).

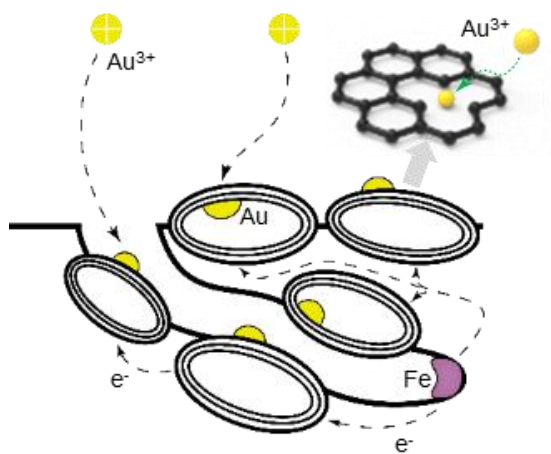
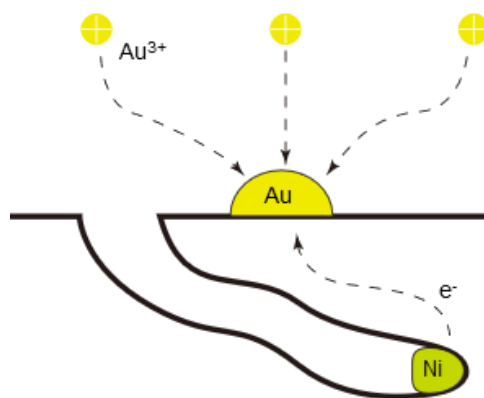
a**b**

Fig.S15. Schematic illustrations of galvanic replacement reaction on CM-hy-C (a) and hy-C (b).

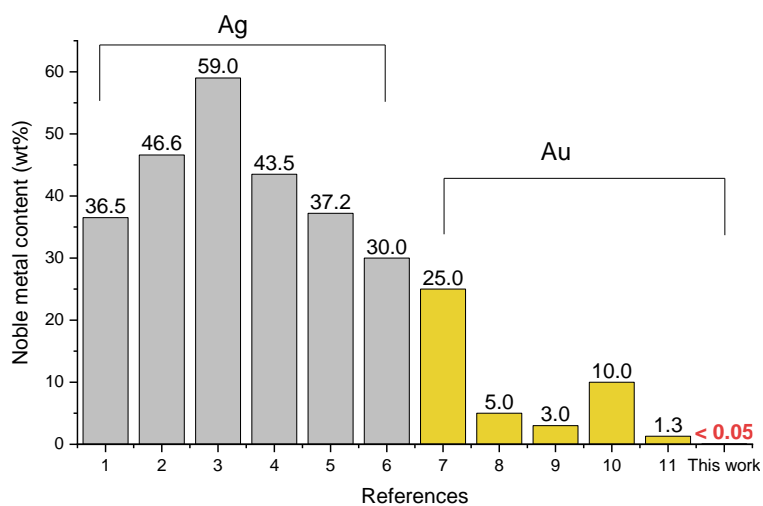
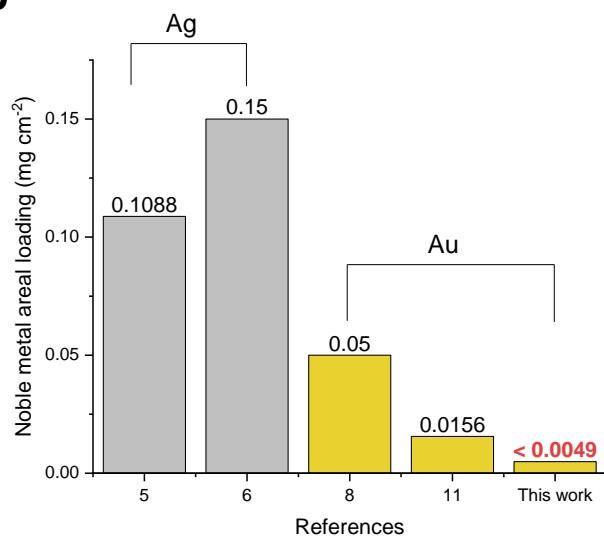
a**b**

Fig.S16. Comparison of noble metal (Ag and Au) content (a) and areal mass loading (b) with recent published studies which developed the Li host matrix decorated with lithiophilic heterometals

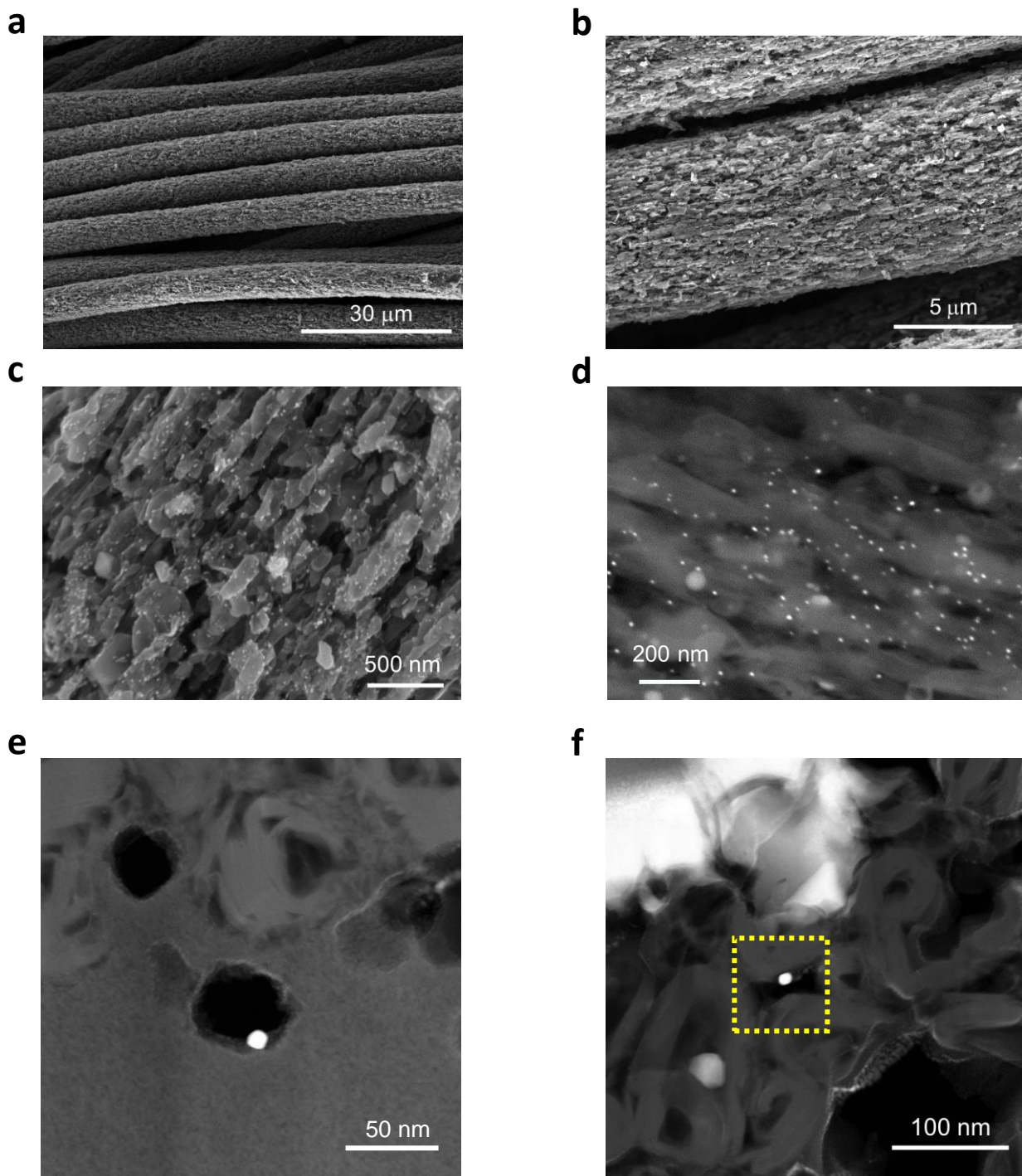


Fig.S17. a-d, SEM images of GR|CM-hy-C in low magnification (a and b) and high magnification (c and d). e,f, Magnified HAADF-STEM images of GR|CM-hy-C in Fig.3e and h. The yellow dot-lined boxes indicate the Au nano-dots placed in the nano-channel (e) and on the surface of graphitic shell (f).

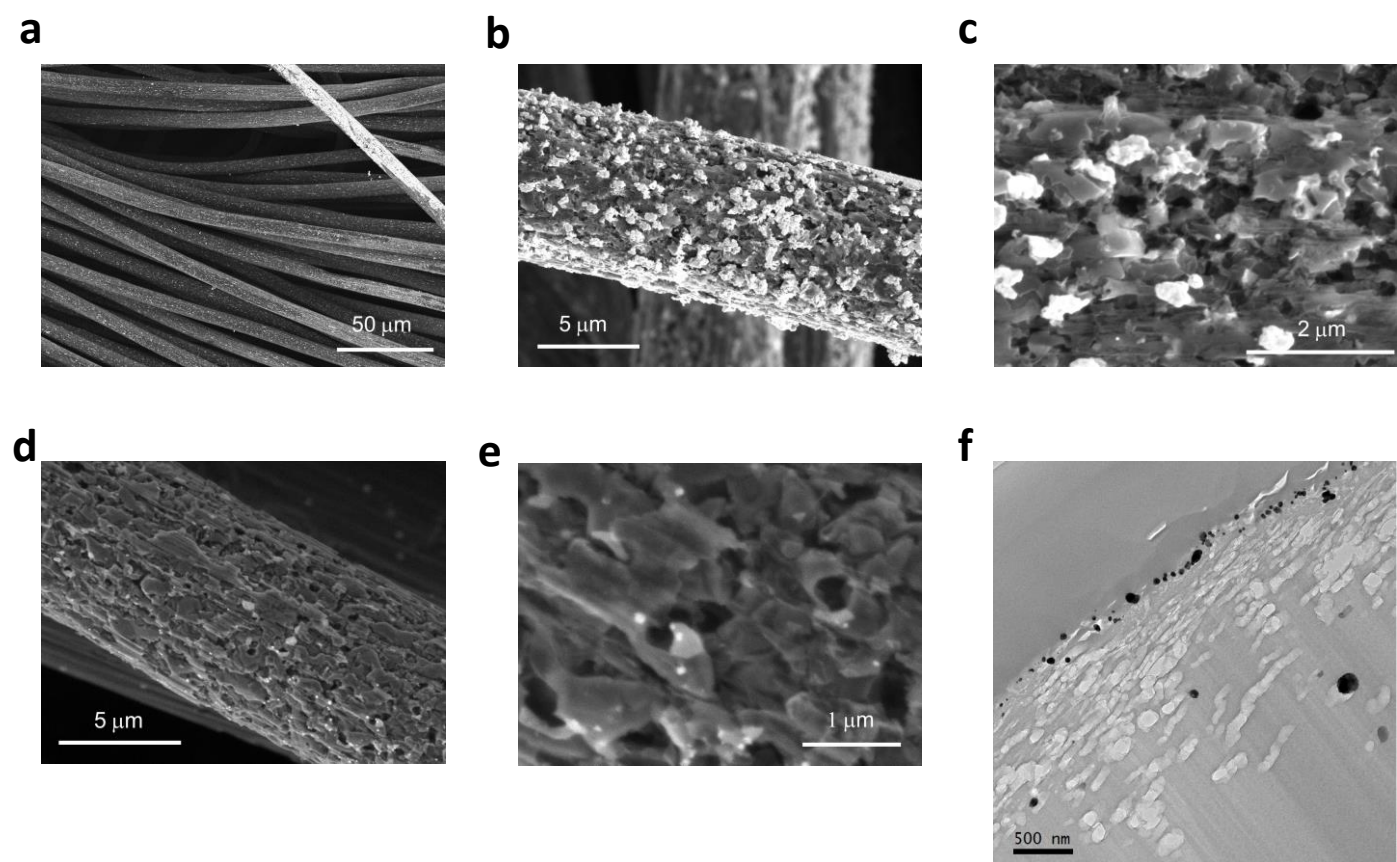


Fig.S18. a-e, SEM images of GR|hy-C in low magnification (a), Au-rich side (b and c), and Au-poor side (d and e). f, HAADF-STEM image of cross-sectional GR|hy-C.

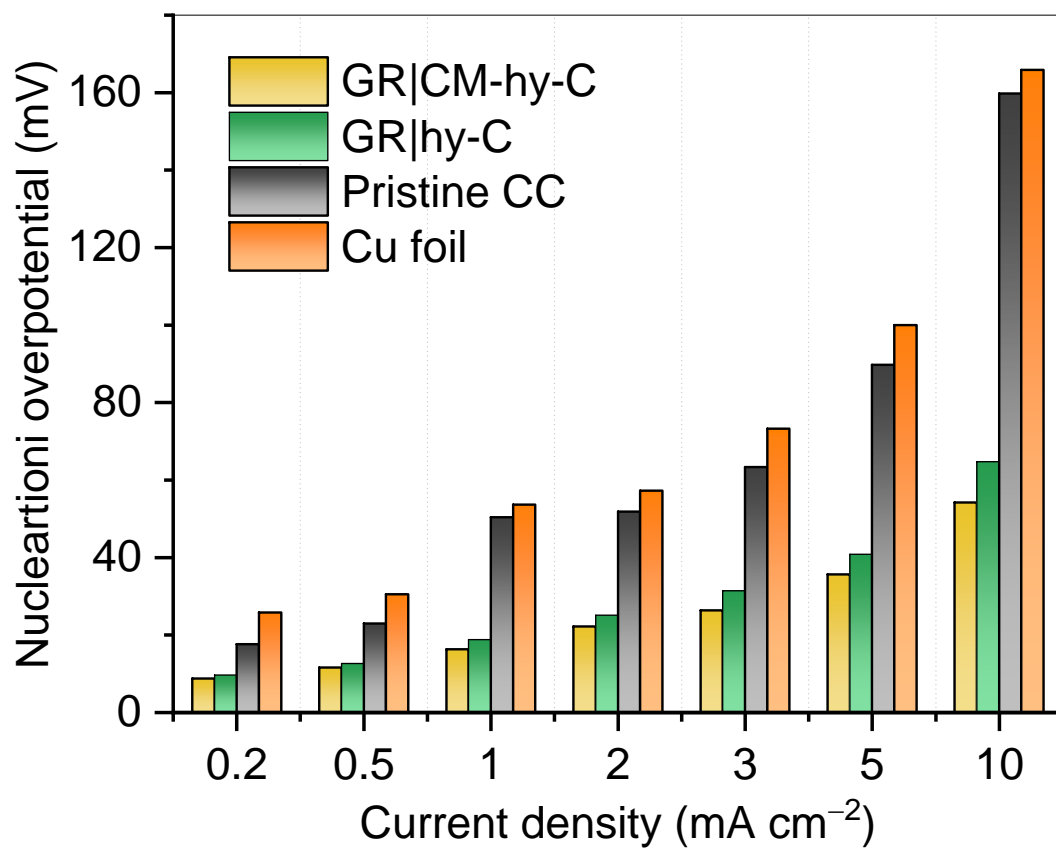


Fig.S19. Li nucleation overpotential for each sample under various applied current densities from 0.2 to 10 mA cm⁻².

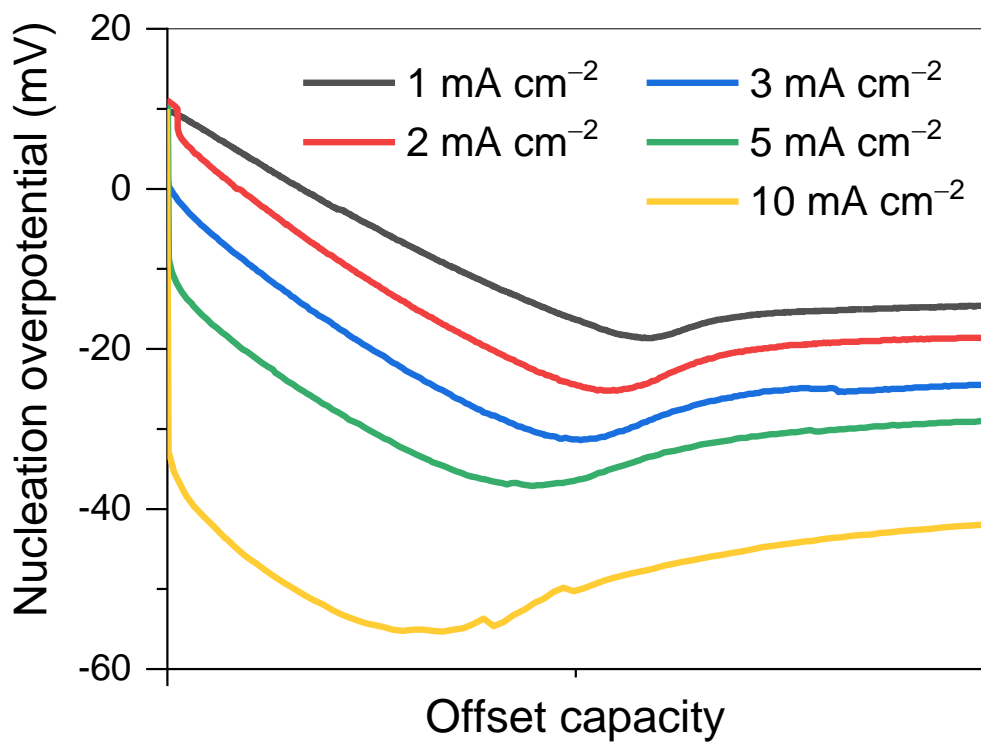


Fig.S20. Li nucleation overpotential of GR|CM-hy-C under various applied current densities.

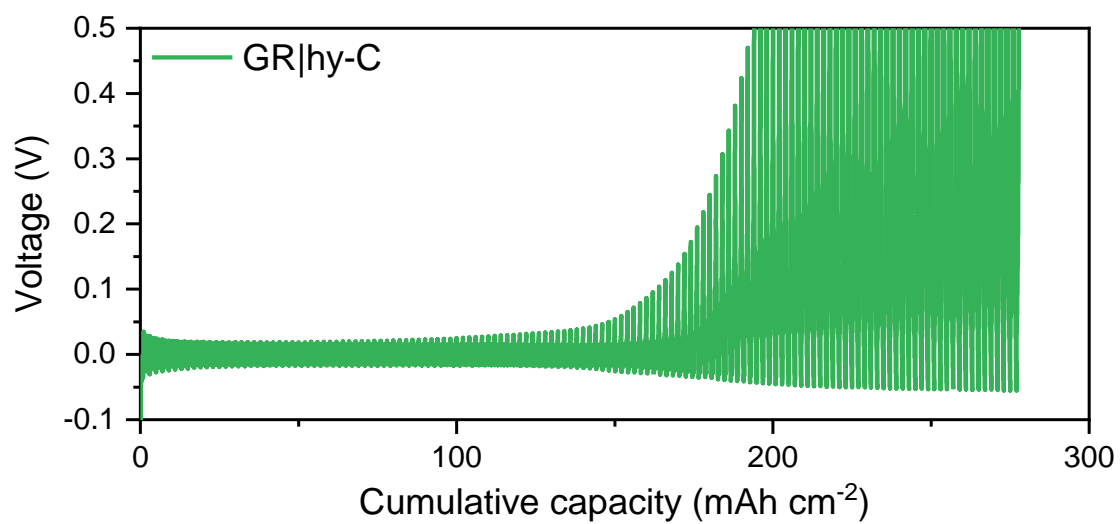


Fig.S21. Li plating/stripping test for GR|hy-C. 2.0 mA cm⁻² of current density was applied for both Li plating and stripping step.

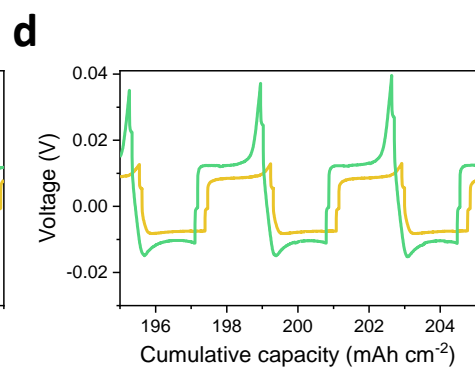
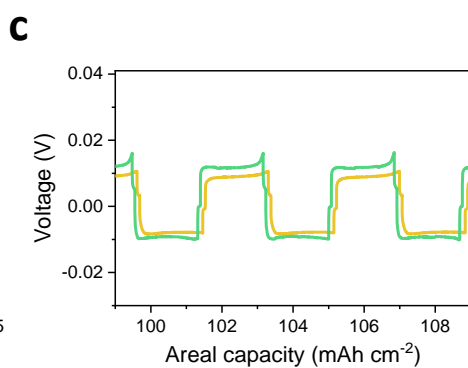
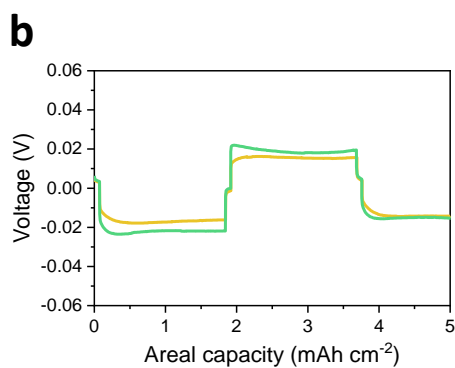
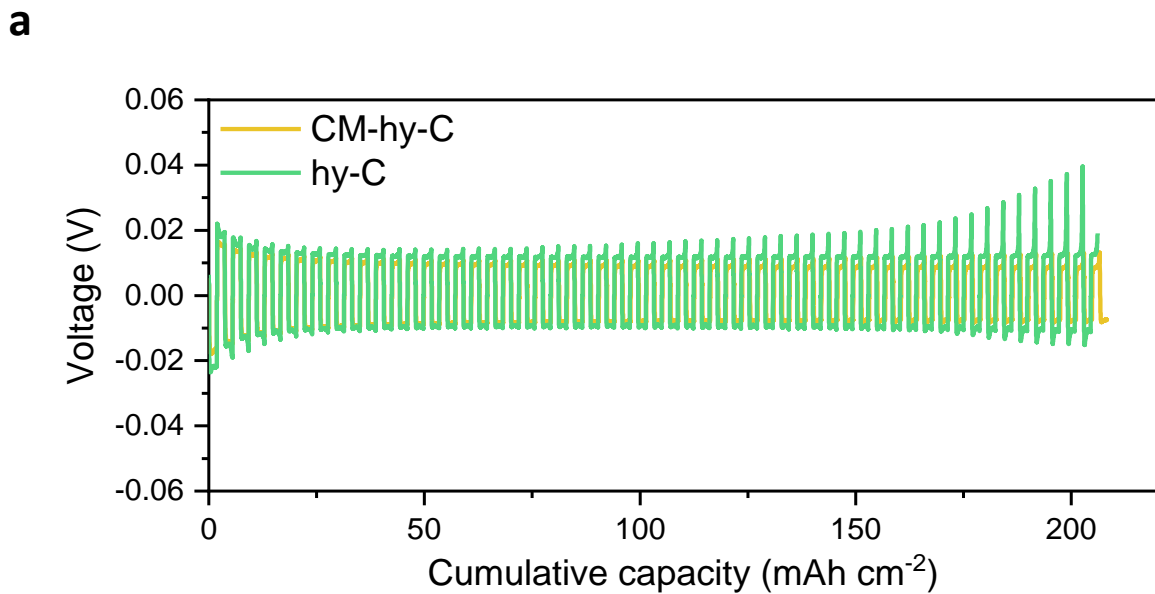


Fig.S22. a, Li plating/stripping test for CM-hy-C and hy-C. All tests were used 0.5 mA cm^{-2} of current density for both Li plating and stripping step. b-d, Magnified Li plating/stripping plot for each sample.

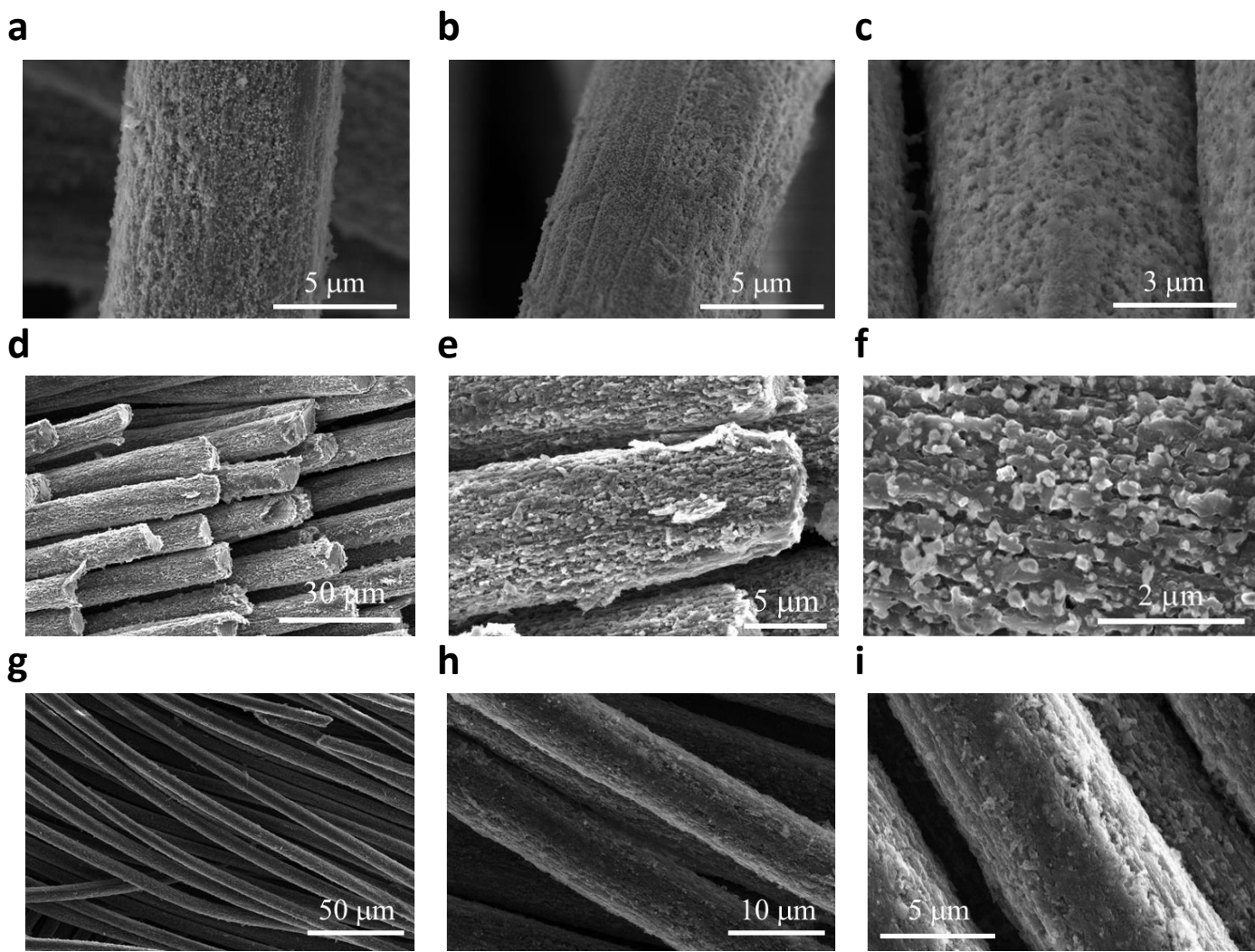


Fig.S23. SEM images of GR|CM-hy-C after 0.5 mAh cm⁻² (a-c), 1.0 mAh cm⁻² (d-f), and 2.0 mAh cm⁻² (g-i) of Li deposition.

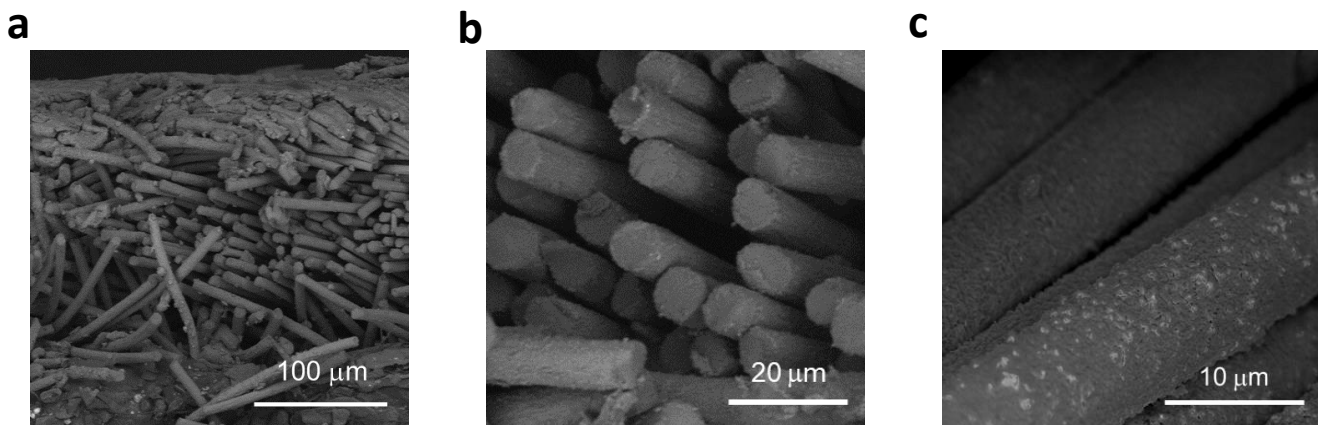


Fig.S24. a-c, SEM images of GR|CM-hy-C after 3.5 mAh cm⁻² of Li deposition.

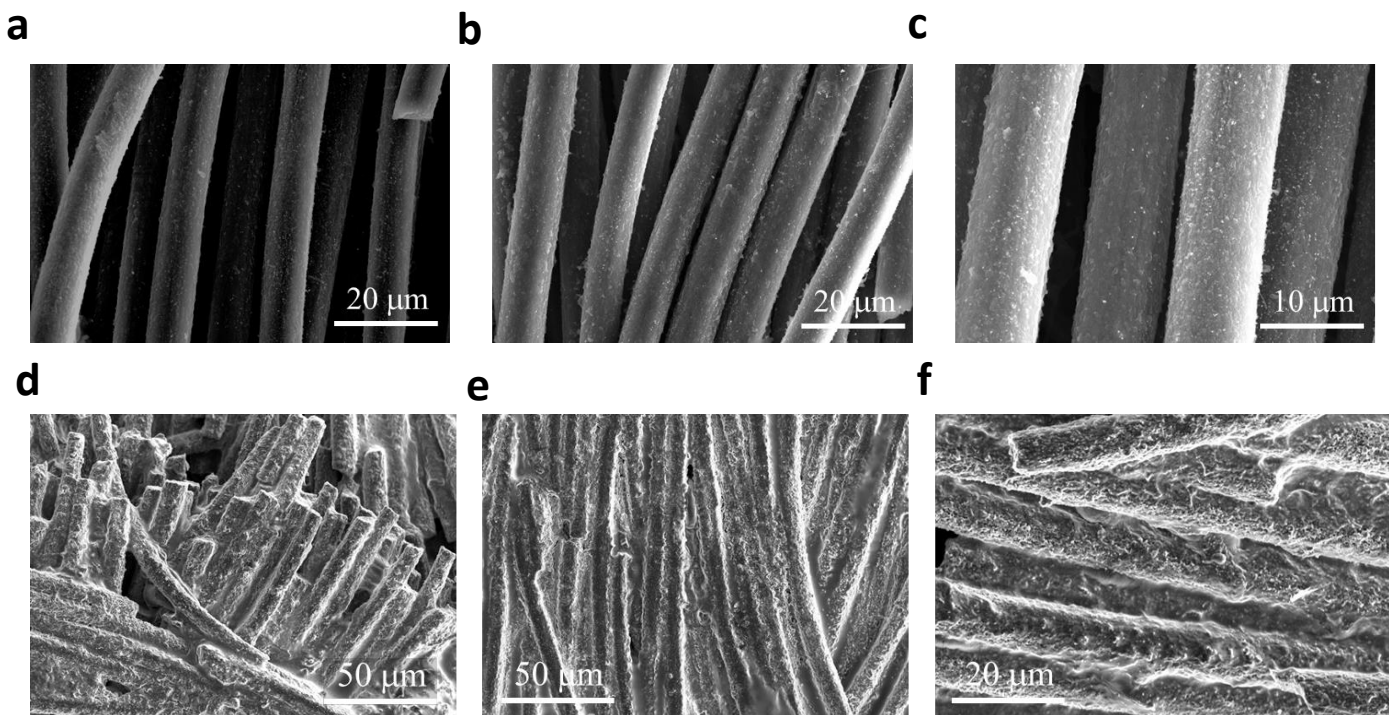


Fig.S25. SEM images of GR|CM-hy-C after 3.0 mAh cm⁻² (a-c) and 5.5 mAh cm⁻² (d-f) of Li deposition.

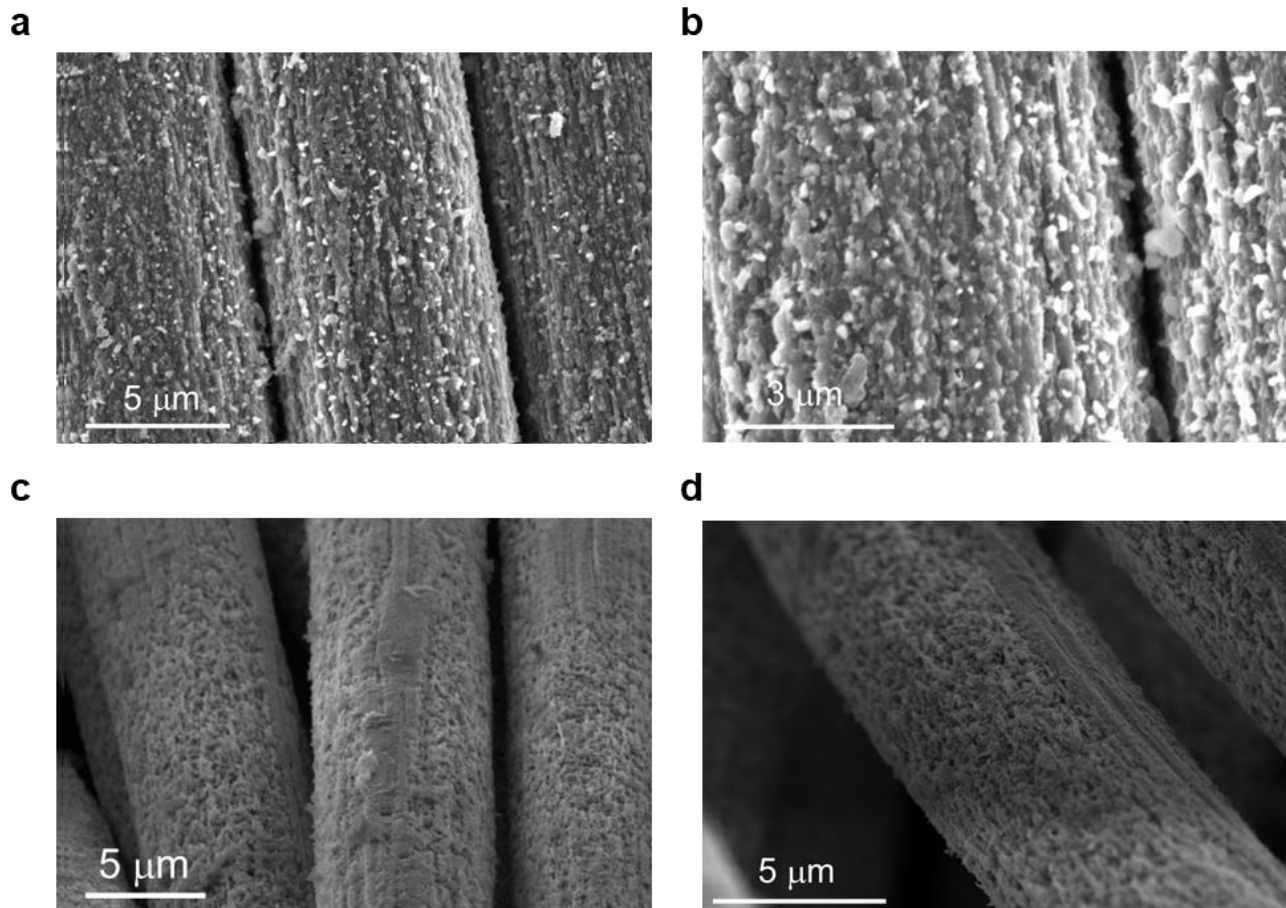


Fig.S26. a-d, SEM images of Li deposited GR|CM-hy-C with 2.0 mAh cm^{-2} (a and b) and 0.5 mAh cm^{-2} of Li residue after Li stripping. 3.0 mAh cm^{-2} of Li was deposited on GR|CM-hy-C before the Li stripping process.

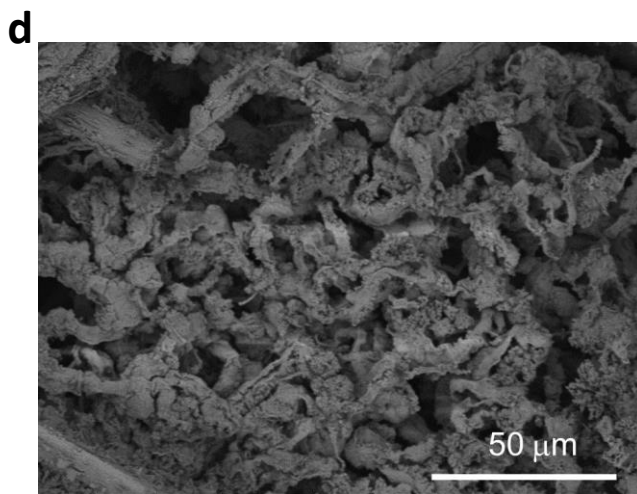
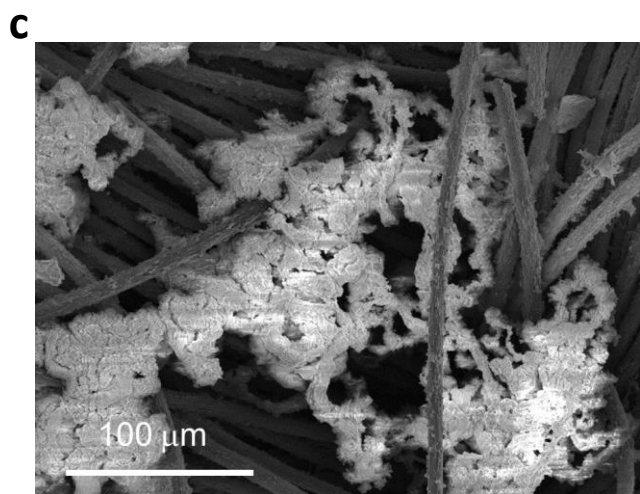
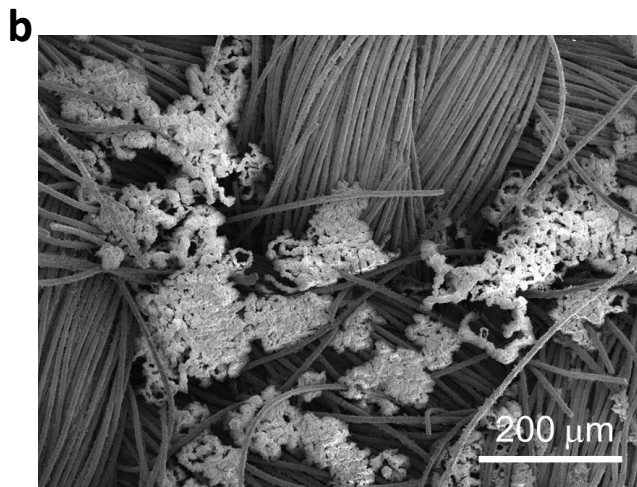
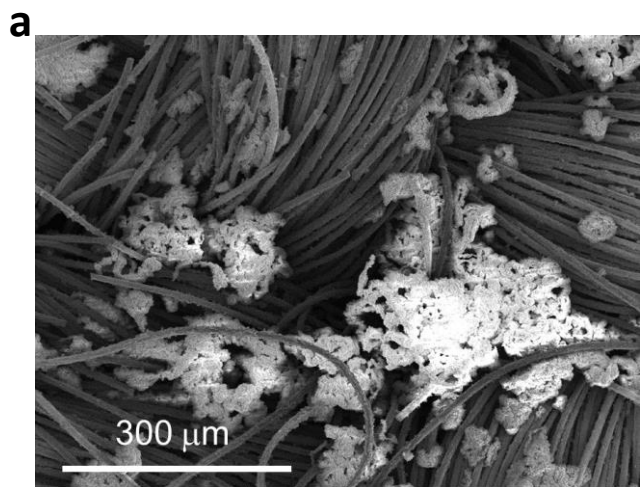


Fig.S27. a-d, SEM images of pristine carbon cloth after Li deposition test. Back-scattered electron SEM of the pristine carbon cloth (d).

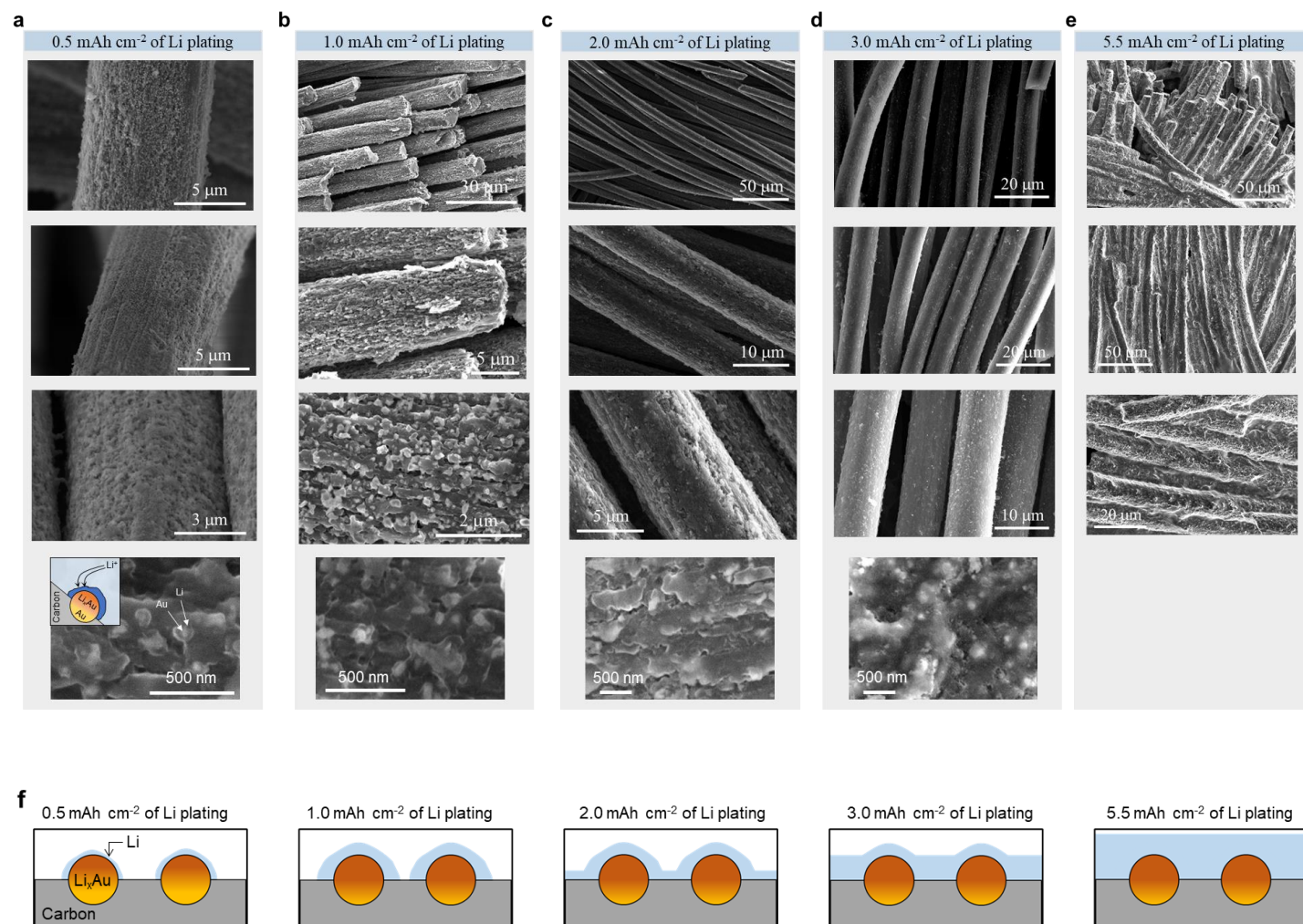


Fig.S28. a-f, Summary of SEM characterization (a-e) for Li deposition behavior analysis on GR|CM-hy-C as various amount of Li plating. Schematic illustrations (f) of Li deposition behavior on GR|CM-hy-C as amount of deposited Li increases.

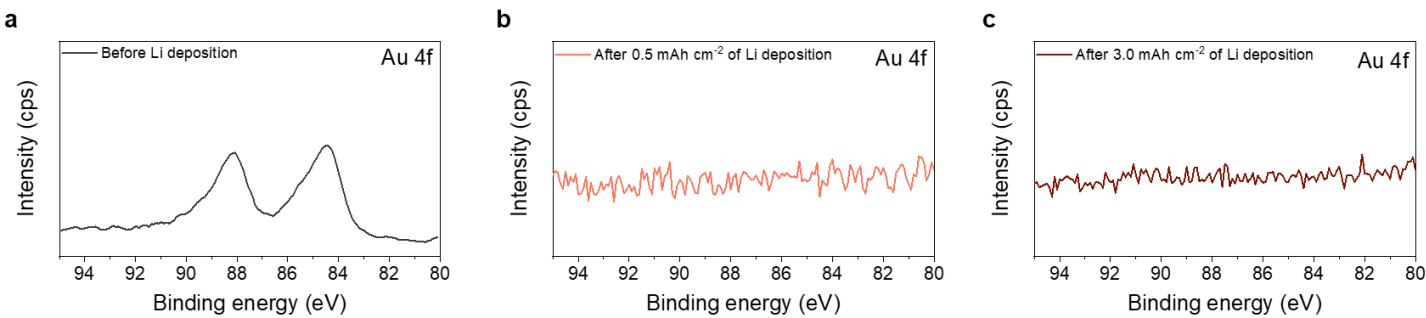


Fig.S29. a-c, XPS analysis for GR|CM-hy-C after various amount of Li deposition. a, Au 4f spectrum of pristine GR|CM-hy-C. b and c, Au 4f spectrum of GR|CM-hy-C after 0.5 mAh cm⁻² (b) and 3.0 mAh cm⁻² of Li deposition

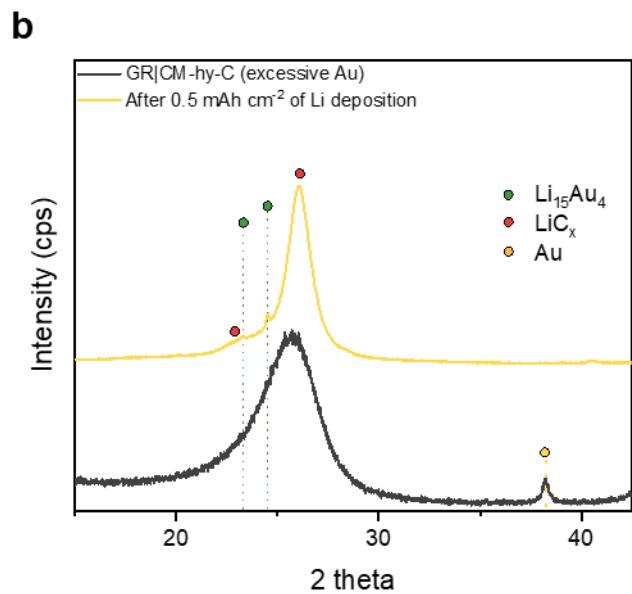
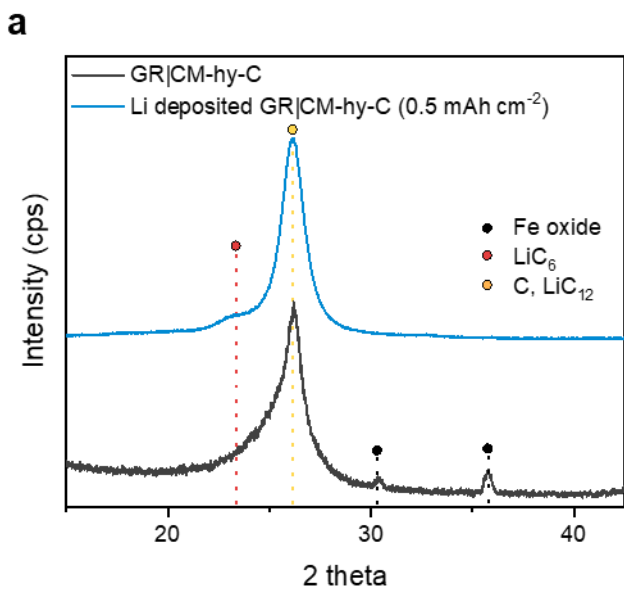


Fig.S30. a and b, XRD analysis for GR|CM-hy-C (a) and excessive Au replaced GR|CM-hy-C (b) with 0.5 mAh cm^{-2} of Li deposition.

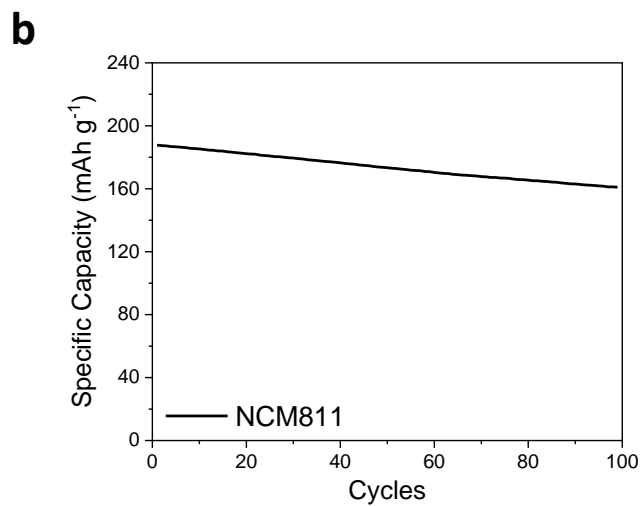
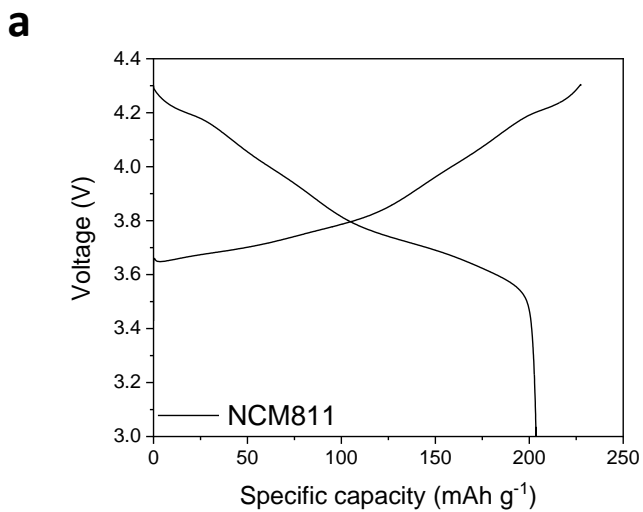


Fig.S31. a, Voltage profile of NCM811 cathode half-cell at the first cycle. b, Cycling performance of NCM811 cathode in half-cell.

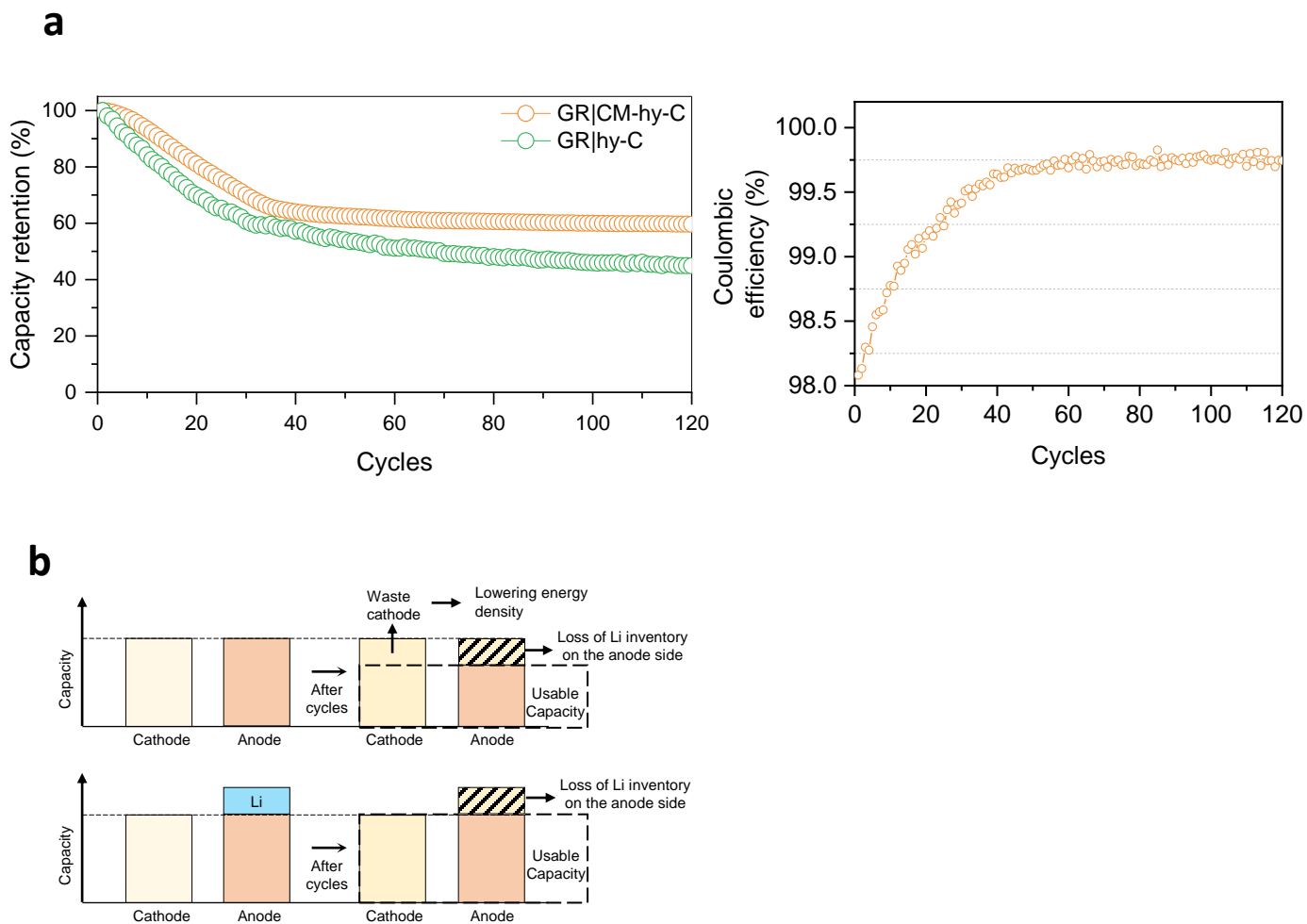


Fig.S32. a, Cycling performance (left) and efficiency (right) of Li-free GR|CM-hy-C full-cell with NCM811 cathode. b, Schematic plot for Li pre-stored full-cell design for higher energy density.

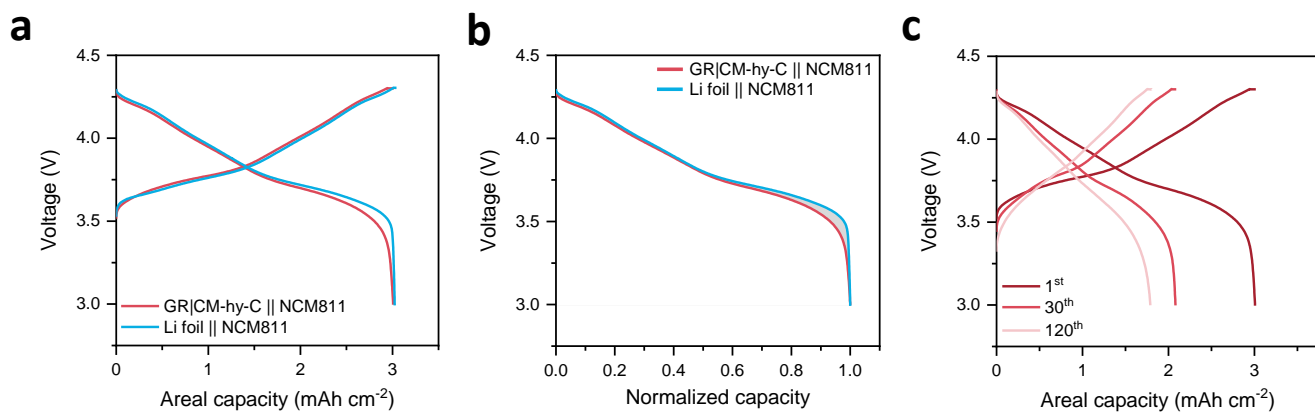


Fig.S33. a, Voltage profiles of Li-free full-cell cycling test for GR|CM-hy-C. b, Normalized discharge capacity plot to investigate the effect of carbon contribution in cycling. c, Voltage profiles of Li-free GR|CM-hy-C during cycling.

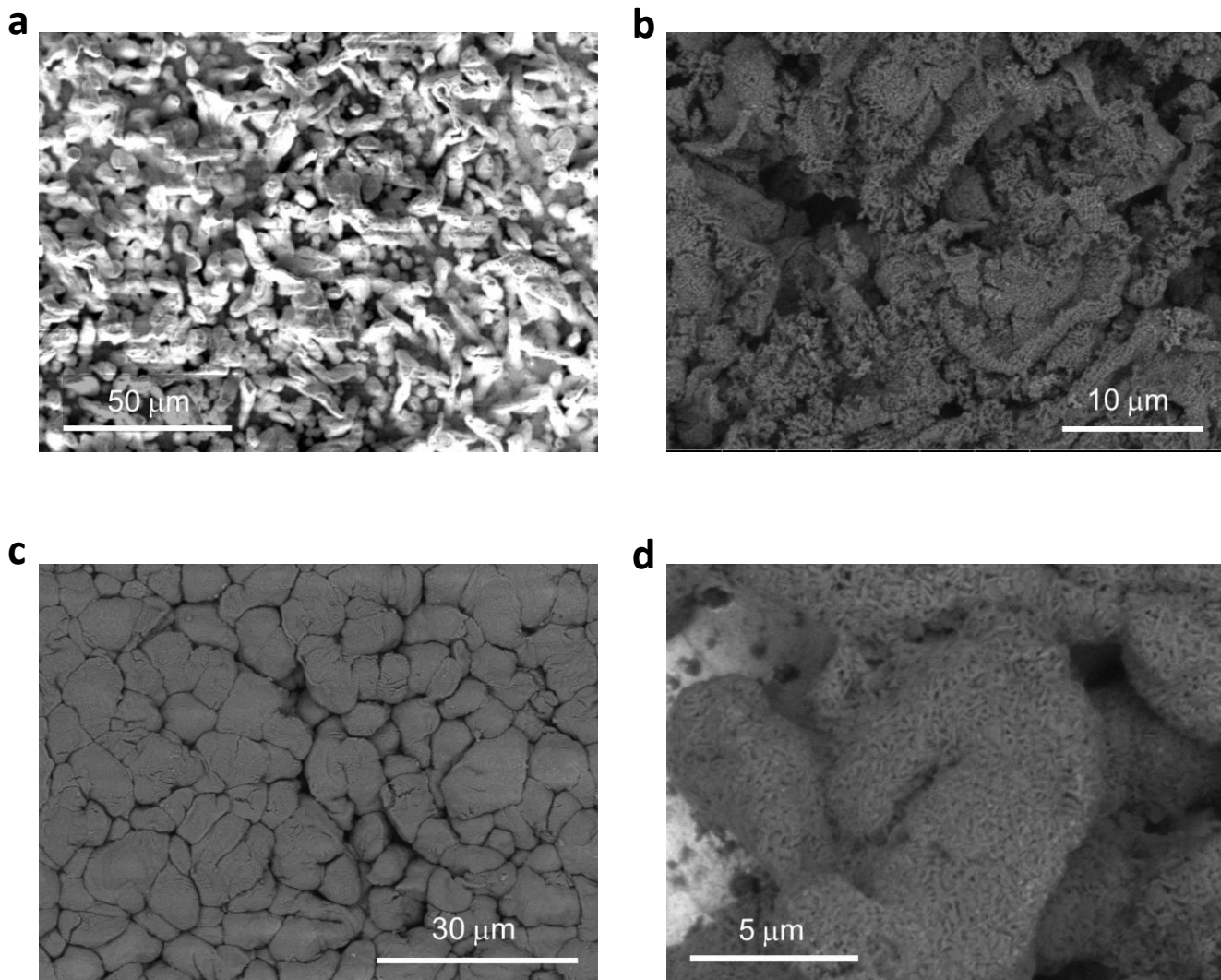


Fig.S34. a-d, SEM images of Cu foil after Li deposition test. Back-scattered electron SEM of the pristine carbon cloth (b-d).

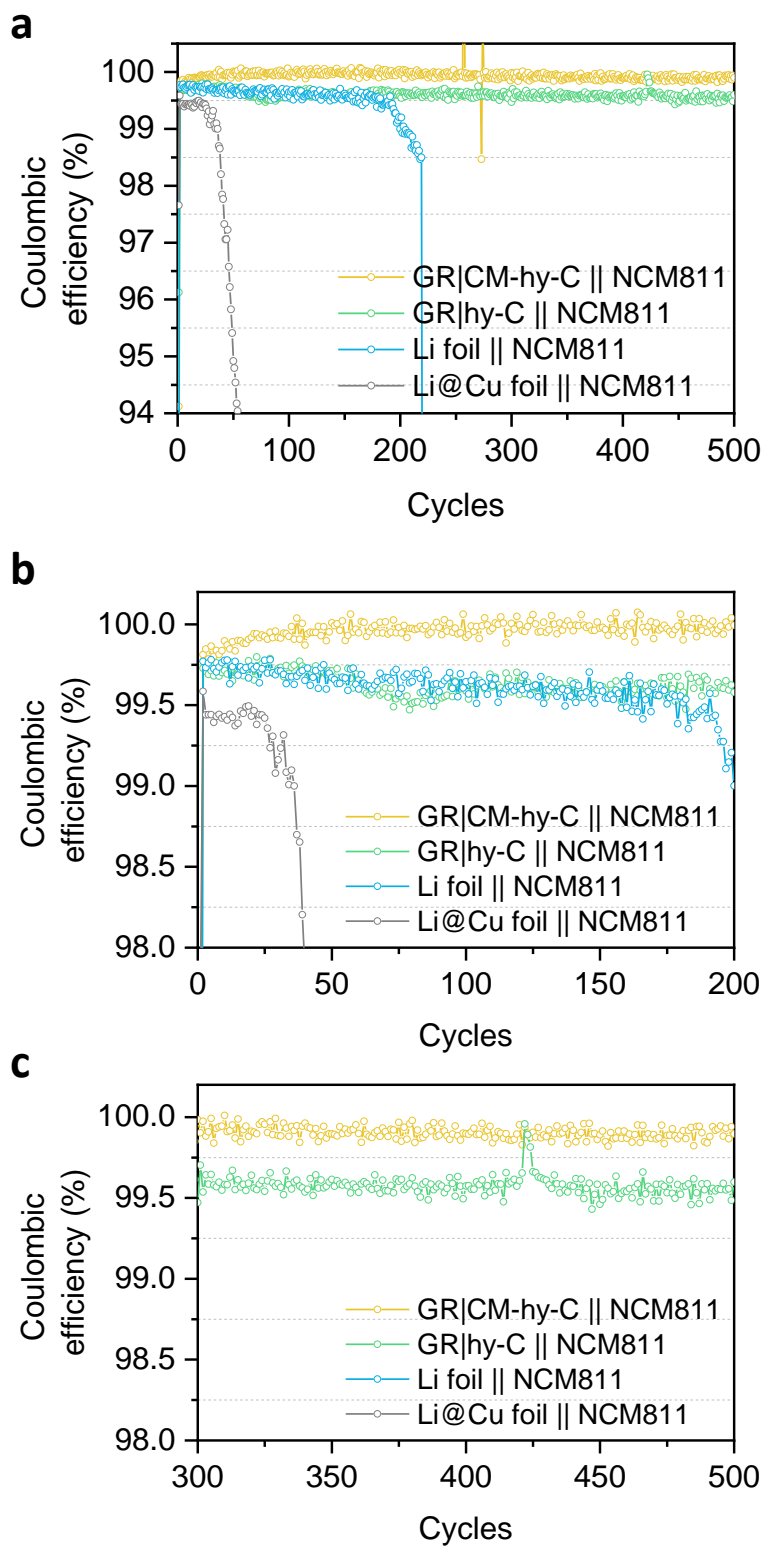


Fig.S35. **a**, Full-cell cycling Coulombic efficiency of each sample. **b,c**, Magnified plot of the cycling efficiency.

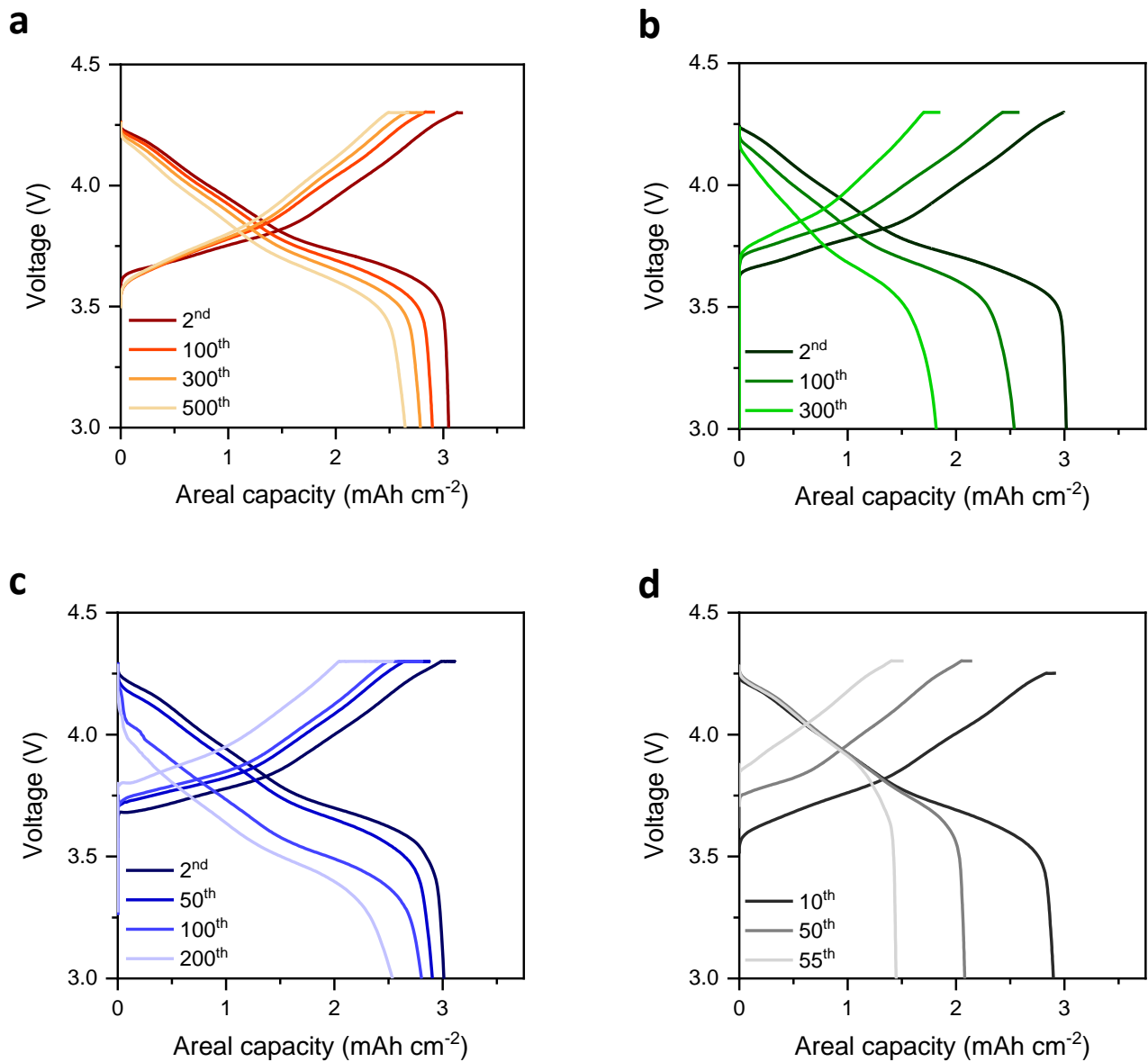


Fig.S36. a-d, Voltage profiles of full-cell cycling test for GR|CM-hy-C (a), GR|hy-C (b), Li foil (c), and Li deposited Cu foil (d).

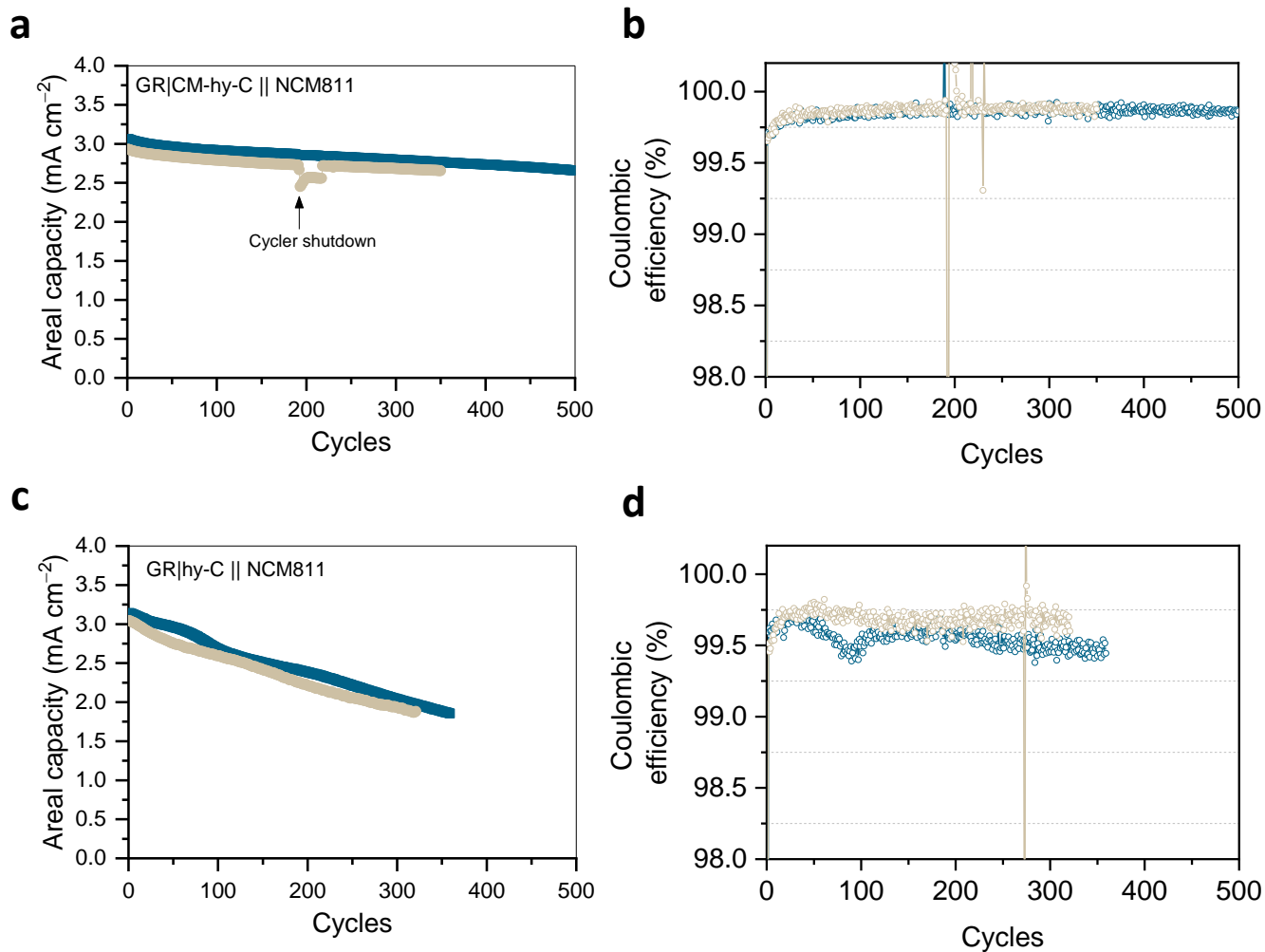


Fig.S37. a-d, Full-cell cycling performance test to confirm the reproducibility of cycling data. (a) Cycle stability and (b) cycling CE of GR|CM-hy-C. (c) Cycle stability and (d) cycling CE of GR|hy-C.

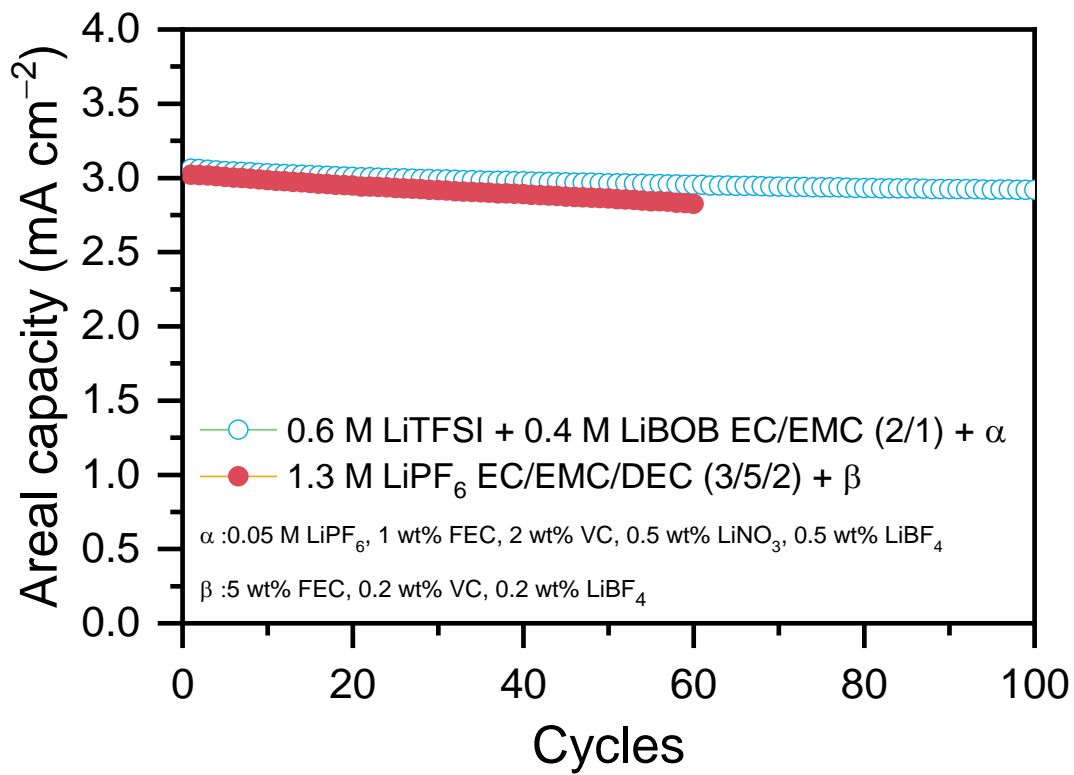


Fig.S38. Full-cell cycling stability of GR|CM-hy-C in different electrolytes.

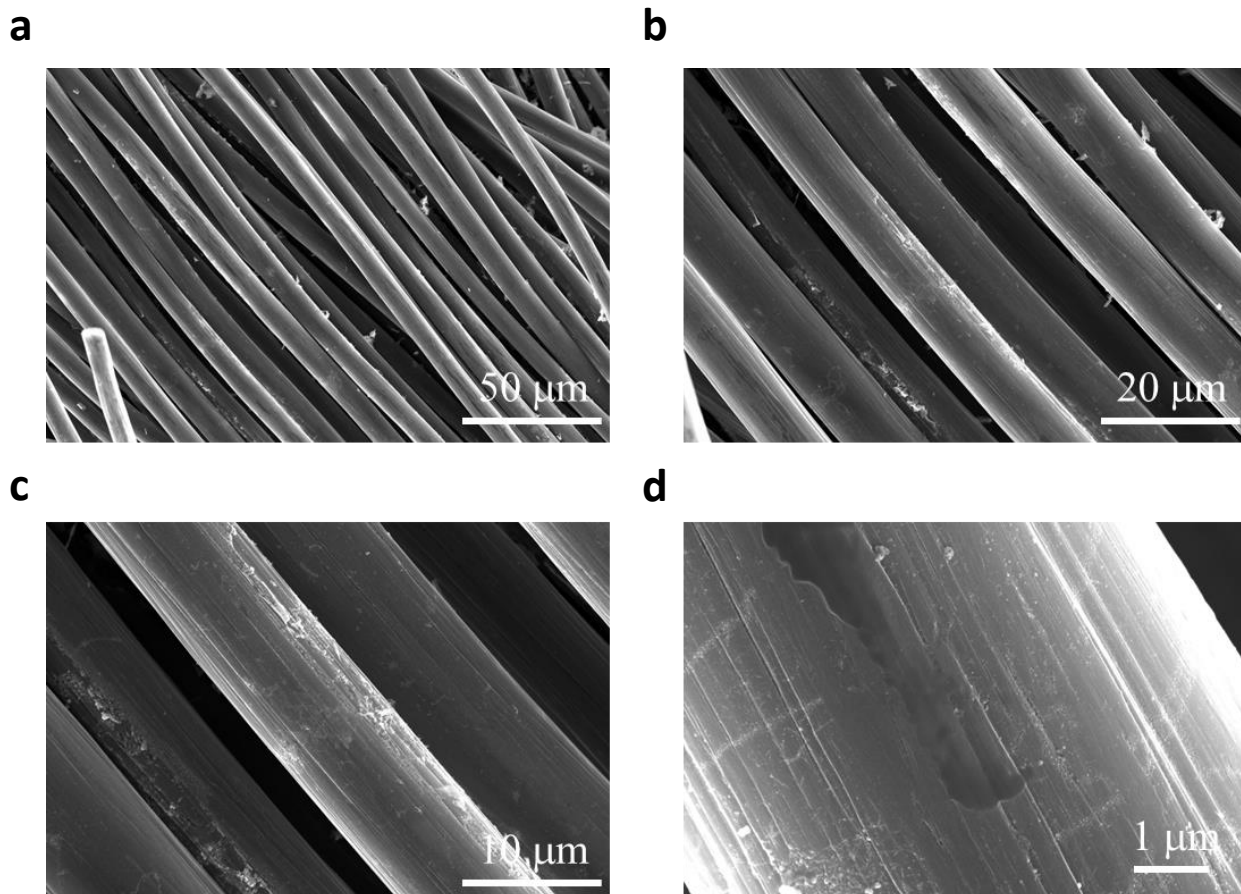


Fig.S39. a-d, SEM images of Fe particle coated carbon cloth synthesized without the catalytic hydrogenolysis reaction.

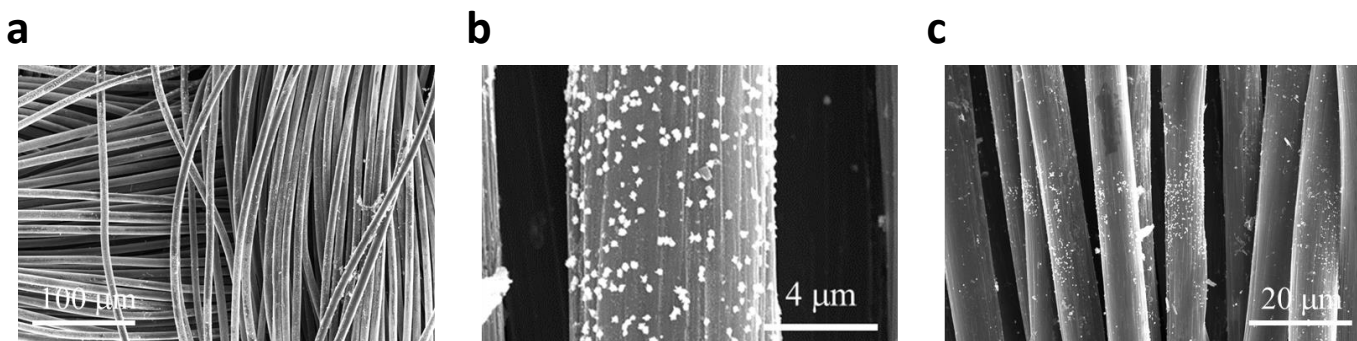


Fig.S40. a-c, SEM images of galvanic replaced Fe particle coated carbon cloth (GR|C) synthesized without the catalytic hydrogenolysis reaction.

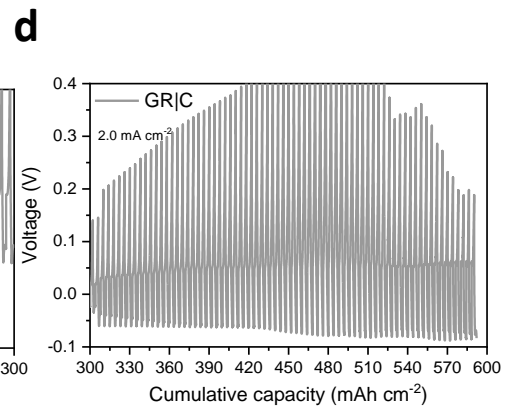
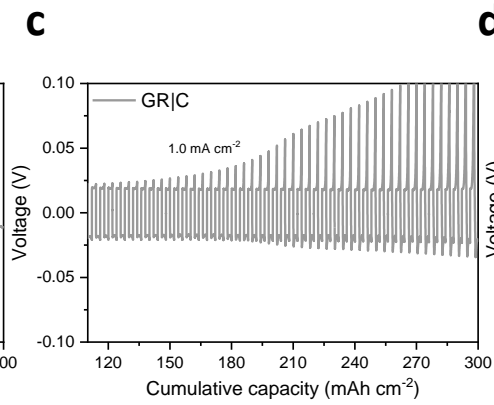
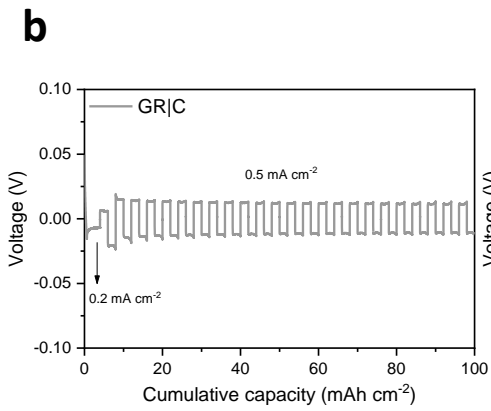
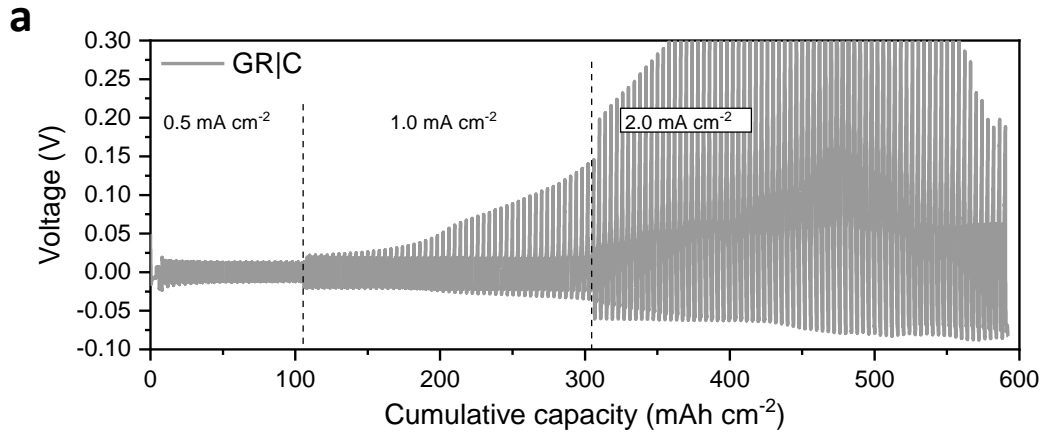


Fig.S41. a-d, Li plating/stripping behavior of GR|C at various current densities (a). Magnified voltage plot under various current density applied (b-d).

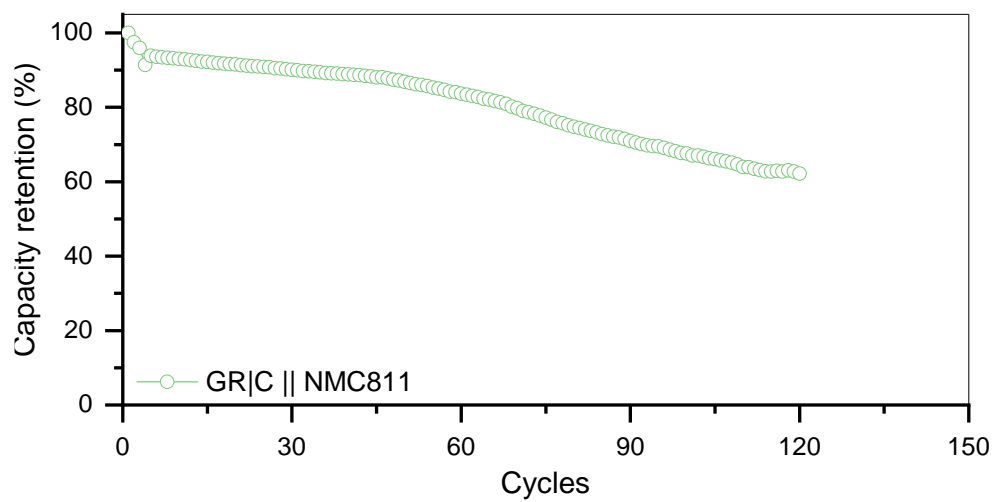


Fig.S42. Full-cell evaluation of GR|C with NMC811 cathode. 2.0 mAh cm⁻² of Li was pre-stored on the GR|C.

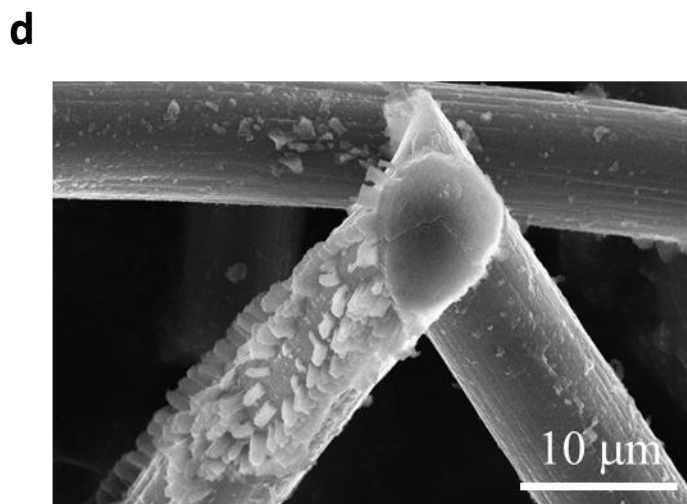
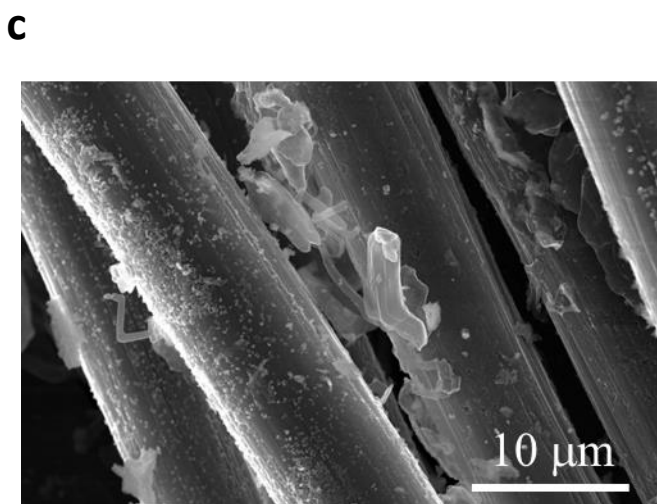
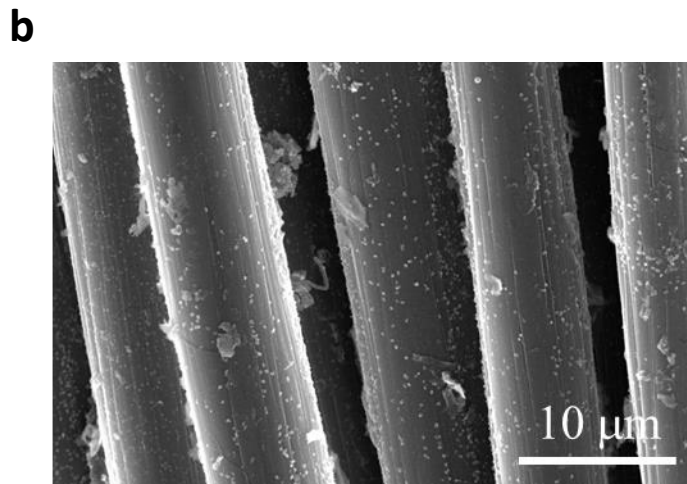
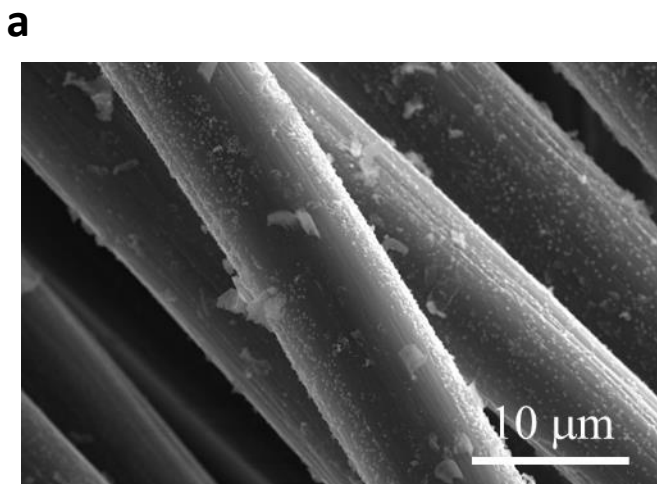
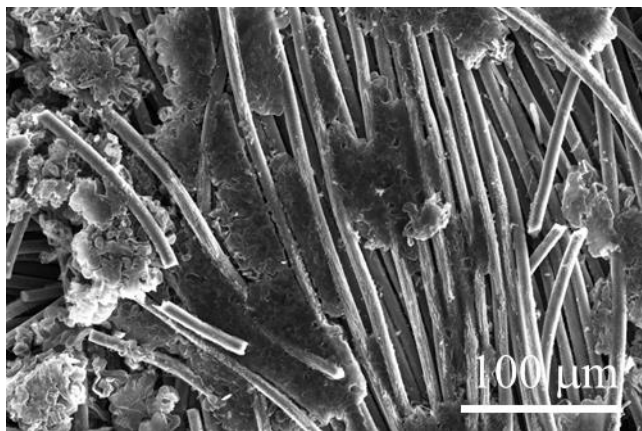


Fig.S43. a-d, SEM images of GR|C after 0.5 mAh cm⁻² of Li deposition.

a



b

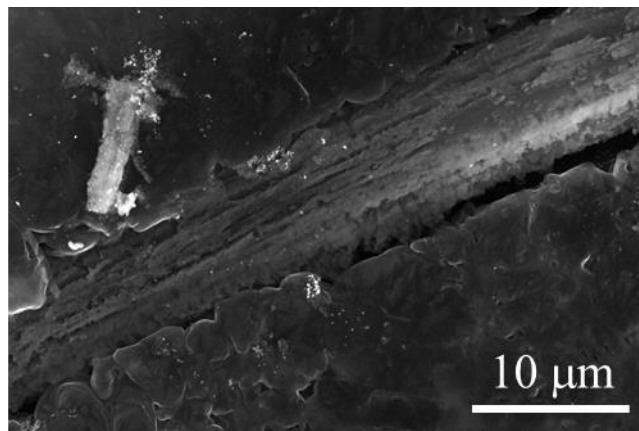


Fig.S44. a-d, SEM images of GR|C after 1.5 mAh cm⁻² of Li deposition.

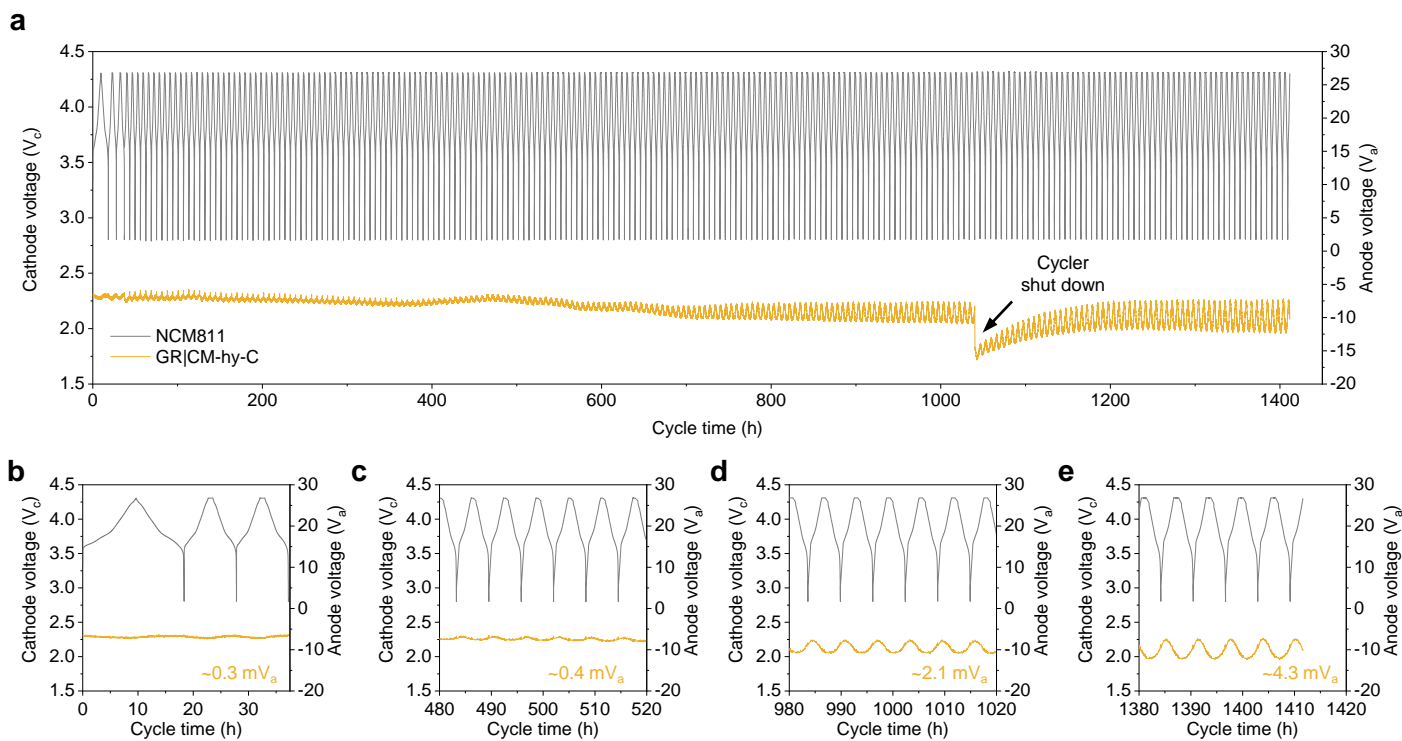


Fig.S45. a, 3-electrode evaluation of pouch-type full-cell with a Li metal reference electrode. **b-e**, magnified plot of full-cell cycling test in 3-electrode evaluation.

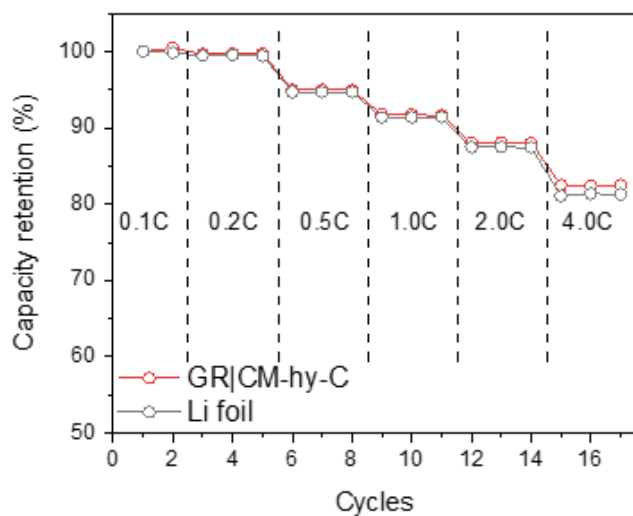
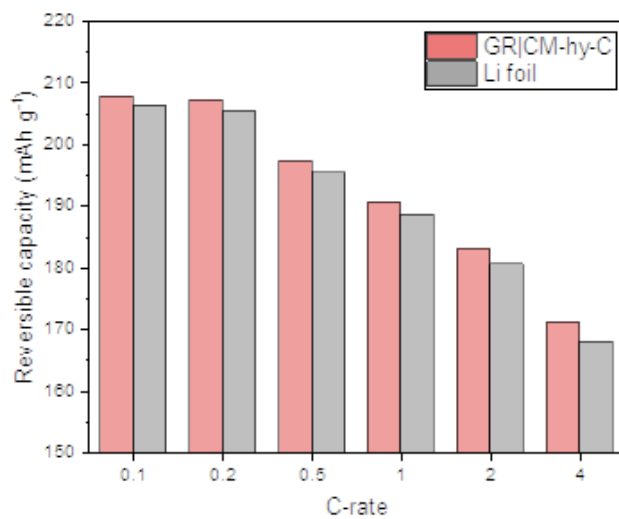
a**b**

Fig.S46. a, Rate capability of the full-cell using GR|CM-hy-C and pristine Li foil as anode electrode. **b**, Reversible specific capacity divided by cathode weight at each current density.

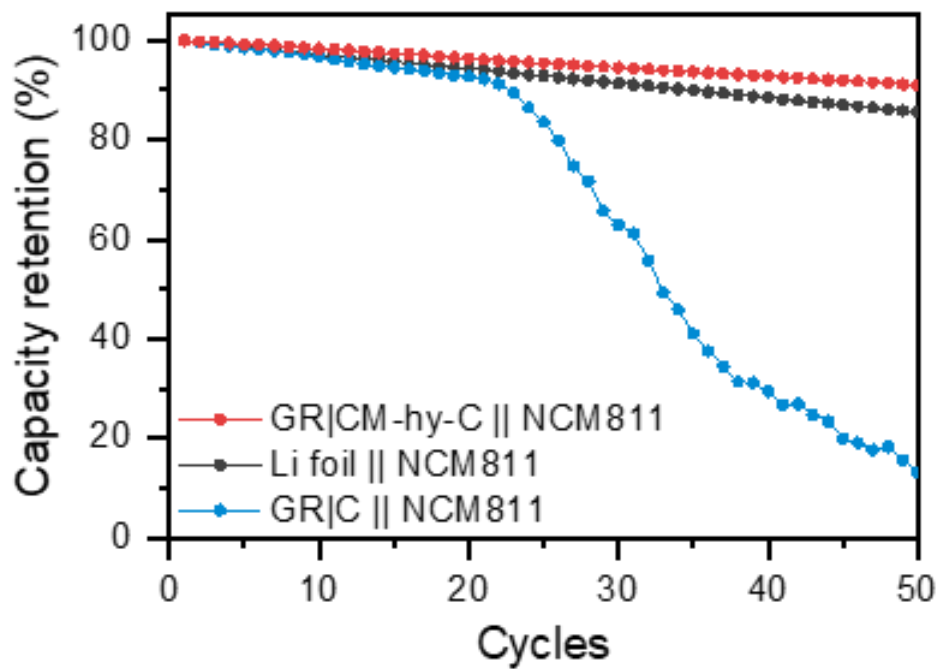


Fig.S47. Cycling performance of each sample at the ambient temperature (60°C)

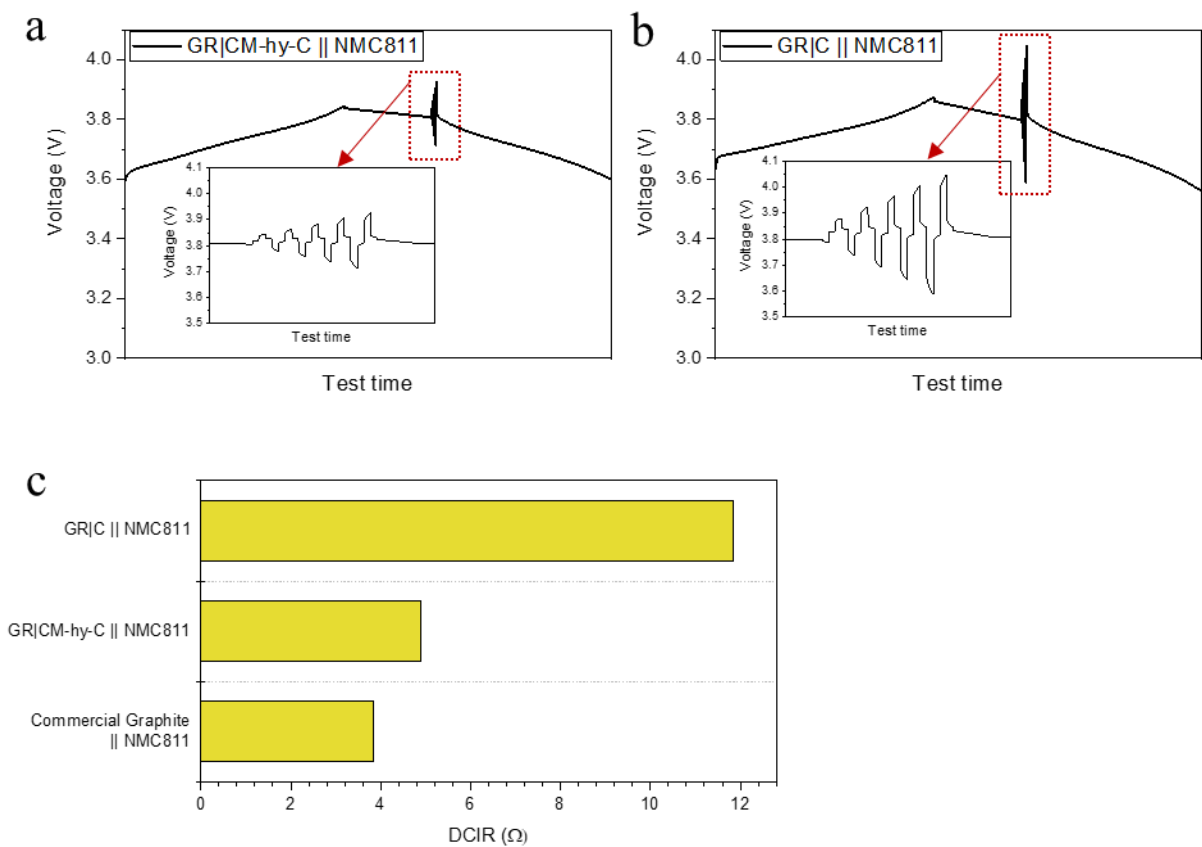


Fig.S48. Voltage profile of pouch-type cells for measuring direct current internal resistance (DCIR) of GR|CM-hy-C (a) and GR}C (b). DCIR values of each sample including commercial graphite cell.

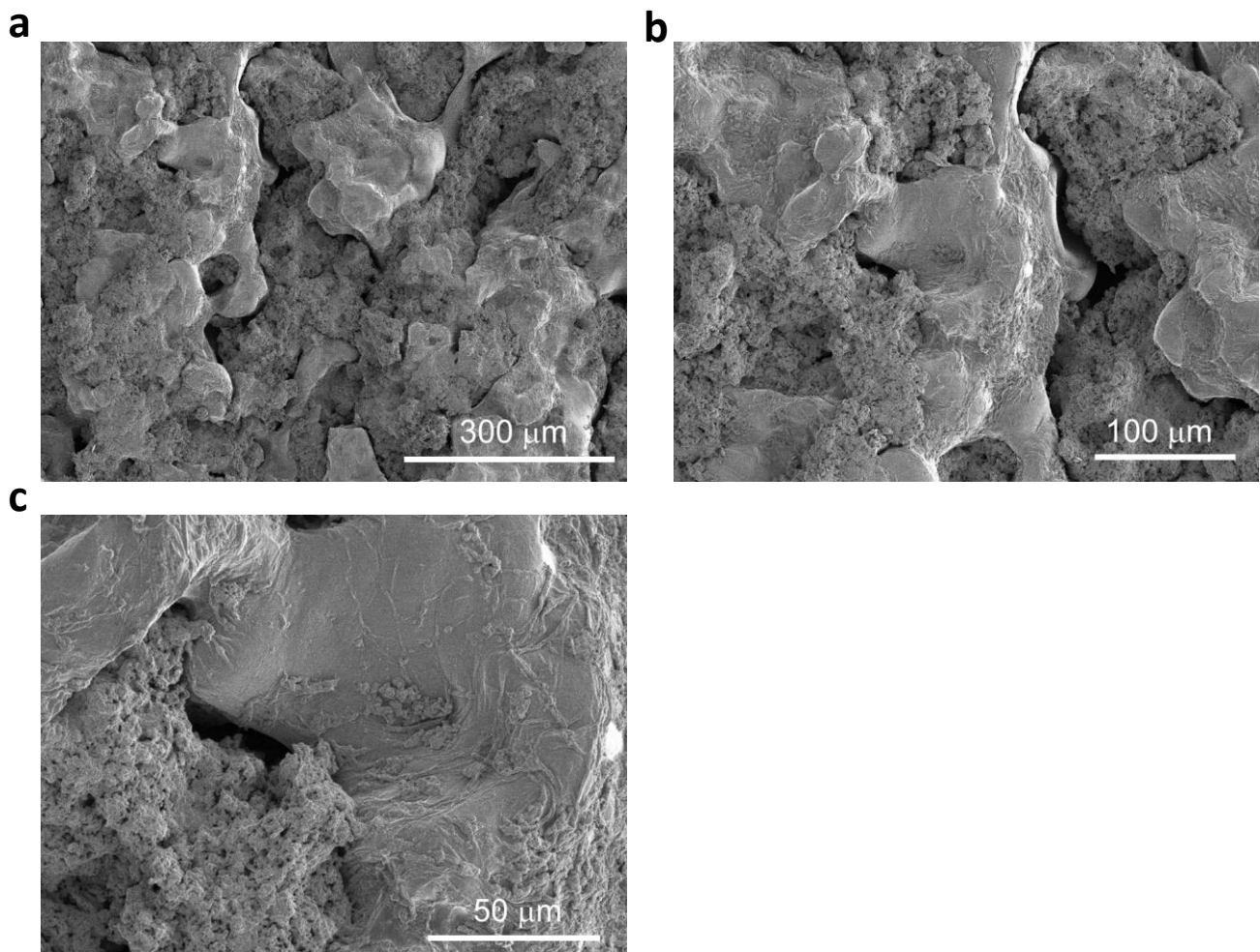


Fig.S49. a-c, Post-cycling SEM images of pristine Li foil in the full-cell test after 300 cycles.

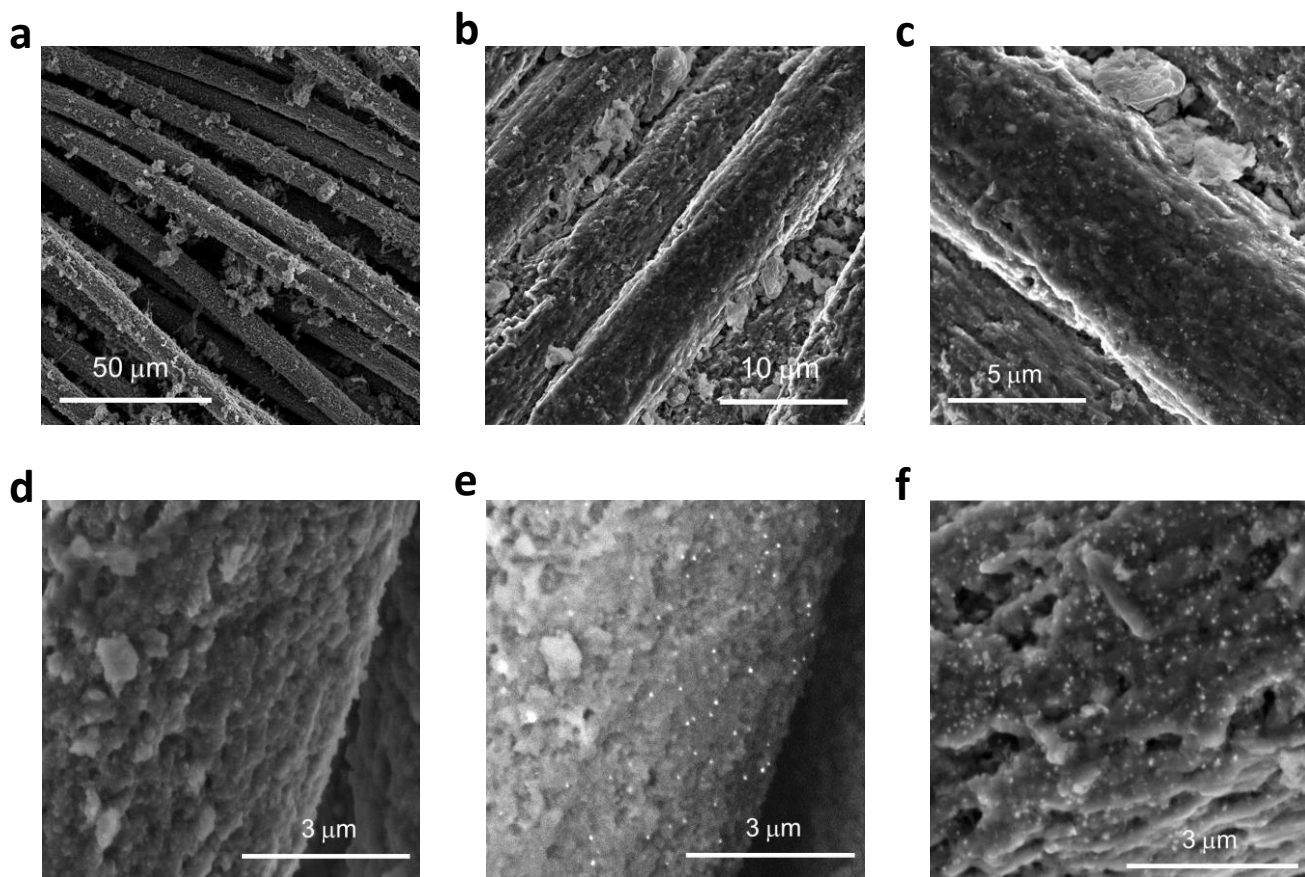


Fig.S50. Post-cycling SEM images of GR|CM-hy-C in the full-cell test after 300 cycles. **a-c**, Low magnified SEM image of post-cycling GR|CM-hy-C. **d-f**, Magnified SEM image of the surface of post-cycling GR|CM-hy-C. (e) is the back-scattered electron SEM image of (d). The Au nano-dots were still maintained on the surface of substrate even after cycling.

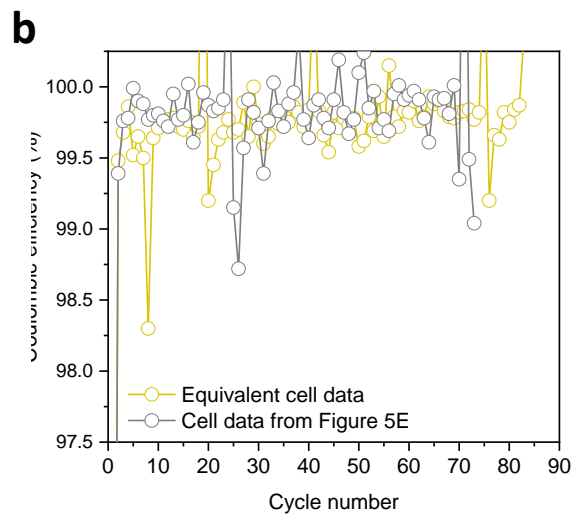
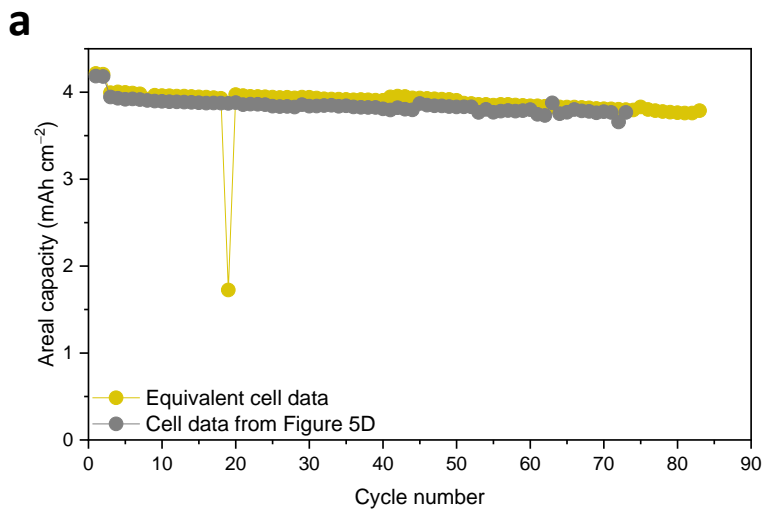


Fig.S51. All-solid-state full-cell cycling performance test to confirm the reproducibility of cycling data. (a) Cycle stability and (b) cycling CE of GR|CM-hy-C.

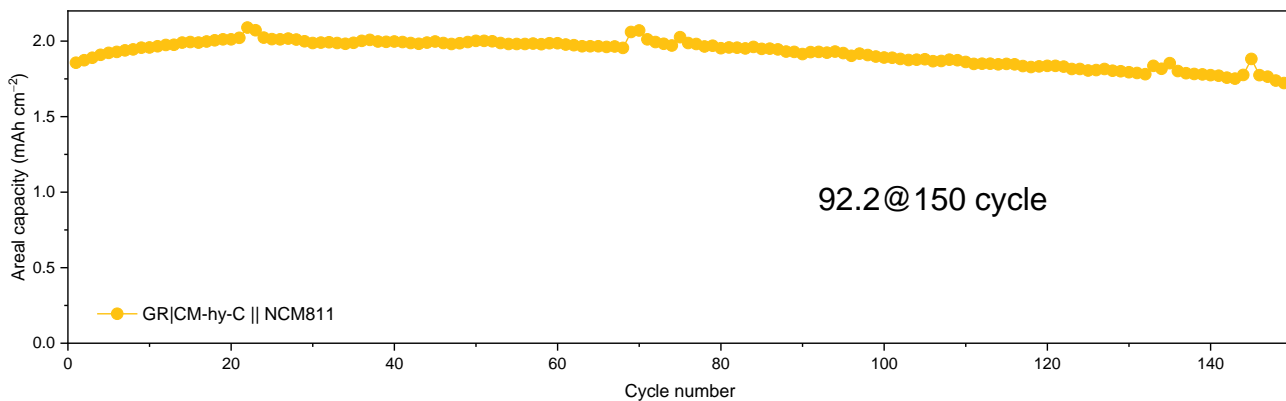
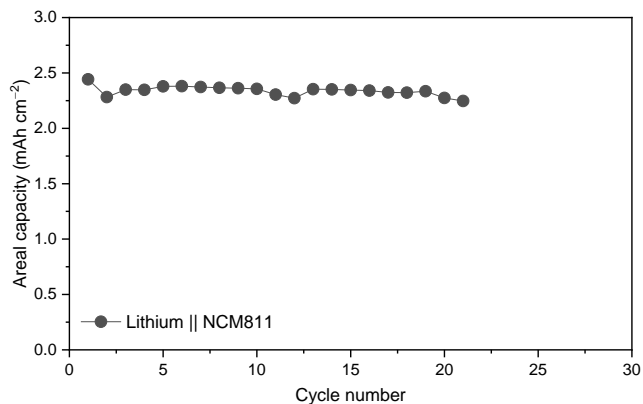
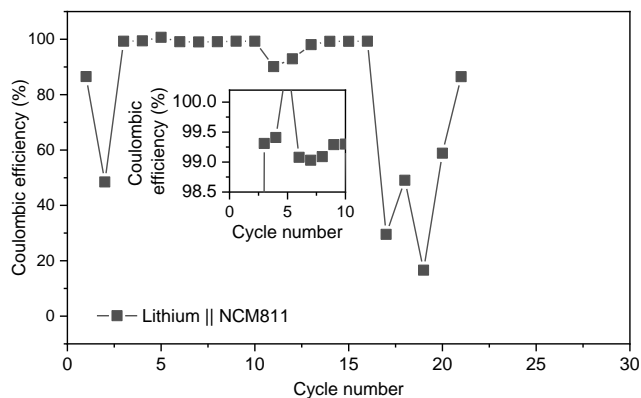
a**b****c**

Fig.S52. Cycling performances (60 °C) of ASSB full-cell in low areal capacity. a, full-cell cycling performance of GR|CM-hy-C||NCM811. b,c, Full-cell cycling performance of lithium||NCM811 (b) and cycling CE (c). The lithium||NCM811 cells had a short-circuit after 15 cycles.

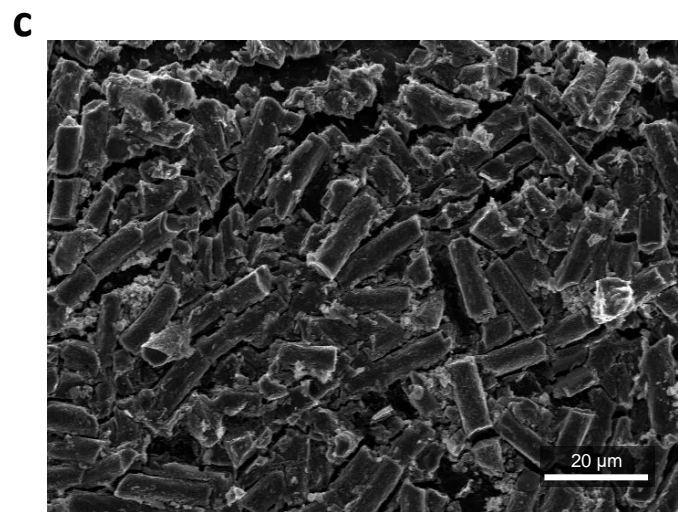
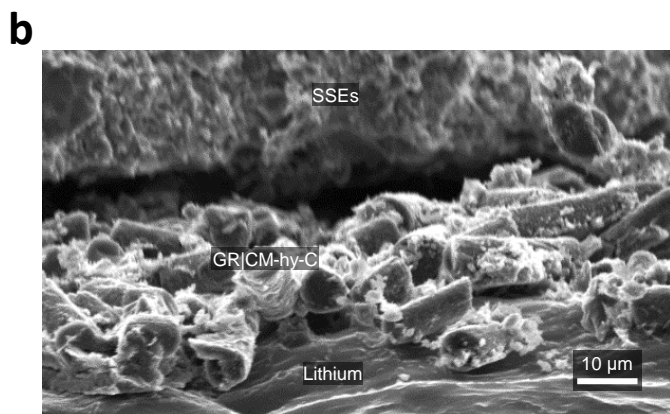
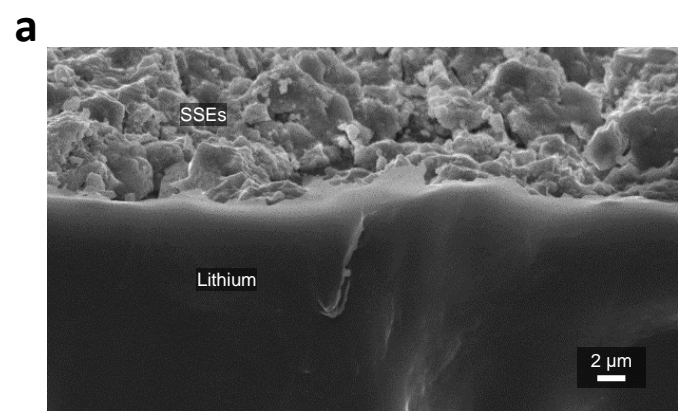


Fig.S53. a,b, Cross-sectional SEM images of pristine Li anode with SSEs (a) and GR|CM-hy-C interlayered Li anode with SSEs (b). c, SEM images of GR|CM-hy-C interlayered Li anode in top-view.

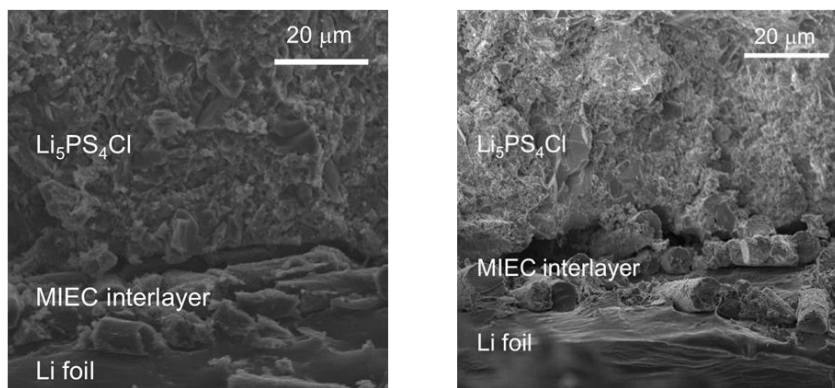
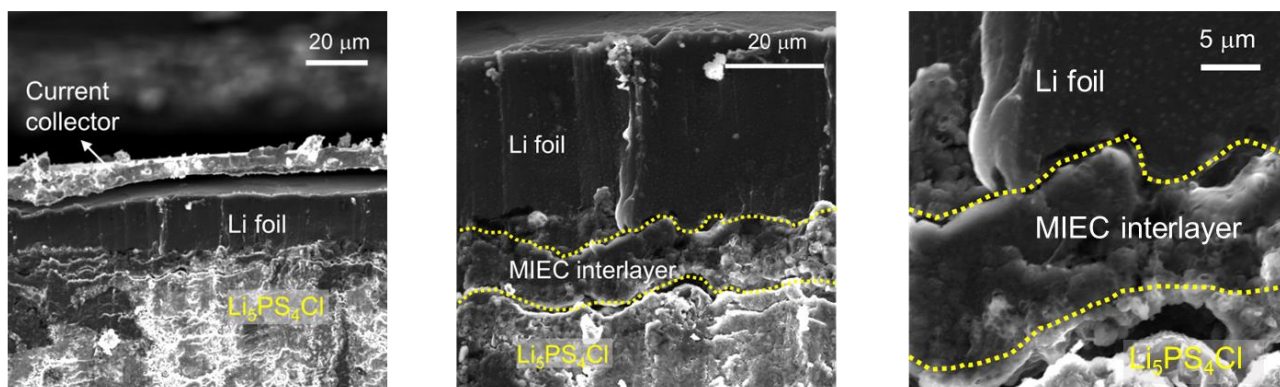
a**b**

Fig.S54. a, Cross-sectional SEM images of GR|CM-hy-C MIEC interlayered Li foil with $\text{Li}_5\text{PS}_4\text{Cl}$ solid-state electrolyte before cycling. b, Cross-sectional SEM images of the MIEC interlayered Li foil after 70 cycles. The preparation of these cross-section sample was done by cutting the sample with a razor blade.

	Surface area (m ² g ⁻¹)
Pristine CC	3.9
GR hy-C	11.8
GR CM-hy-C	11.5

Table S1. BET specific surface area of each sample.

	Energy density (Wh L ⁻¹)	Specific energy (Wh kg ⁻¹)
Commercial graphite	720.9	281.7
GR CM-hy-C	858.4	437.5

Table S2. Energy density and specific energy of commercial graphite cell and GR|CM-hy-C cell. Thickness of current collectors, electrodes, and separator are considered for cell volume calculation. The weight of current collectors, electrodes, separator, and pouch casing are included for calculating total cell weight.

Commercial Graphite cell	Positive (NMC811)	Loading level	21.34	mg cm ⁻²
		Electrode area	7.84	cm ²
		Current collector (Al, 12μm)	0.0254	g
		Electrode weight	0.1927	g
		Electrode density	3.6	g cm ⁻³
		Electrode thickness	71.3	μm
	Separator (13 μm)	Area	10.24	cm ²
		Weight	0.0124	g
	Pouch casing	Area	17.64	cm ²
		Weight	0.03925	g
	Negative (Graphite)	Loading level	13.7	mg cm ⁻²
		Electrode area	9	cm ²
		Current collector (Cu, 15μm)	0.121	g
		Electrode weight (double side)	0.3676	g
		Electrode density	1.6	g cm ⁻³
		Electrode thickness	186.3	μm
	Cell	Average voltage	3.67	V
		Cell capacity	62.72	mAh
		Cell weight	0.817	g
Cell volume		0.3193	cm ³	
GR CM-hy-C cell	Positive (NMC811)	Loading level	21.34	mg cm ⁻²
		Electrode area	7.84	cm ²
		Current collector (Al, 12μm)	0.0254	g
		Electrode weight	0.1927	g
		Electrode density	3.6	g cm ⁻³
		Electrode thickness	71.3	μm
	Separator (13 μm)	Area	10.24	cm ²
		Weight	0.0124	g
	Pouch casing	Area	17.64	cm ²
		Weight	0.03925	g
	Negative (GR CM-hy-C)	Electrode area	9	cm ²
		Electrode weight	0.086	g
		Weight of deposited Li	0.00466	g
		Lithiated electrode weight (double side)	0.0953	g
		Electrode thickness	140	μm
		Average voltage	3.80	V
	Cell	Cell capacity	62.72	mAh
		Cell weight	0.5448	g
		Cell volume	0.2776	cm ³
Separator		2	N	
Number of stacking	Cathode	2	N	
	Anode	1	N	

Table S3. Cell parameters for calculating the energy density and specific energy of commercial graphite cell and GR|CM-hy-C cell.

Ref.	Host materials	ICE before pre-lithiation	Pre-lithiation method	Amount of pre-lithiation (mAh cm ⁻²)	Cathode	Areal cell capacity (mAh cm ⁻²)	Cycle life
[12]	ZnO/Porous carbon	97 %	Electrochemically deposition	4	LiCoO ₂ (LCO)	-	-
[13]	SiO/CNT	75 %	Electrochemically deposition	2	LiFePO ₄ (LFP)	2.0	94.8 % at 50 cycles
[14]	Li/Carbon fiber	-	Li foil	10	LFP	2.0	-
[15]	TiC/C array	80.5 %	Molten Li infusion	-	LFP	0.4	91.3 % at 200 cycles
[16]	Carbonized MOF	-	Electrochemically deposition	5	Li ₄ Ti ₅ O ₁₂ (LTO)	0.32	-
[17]	N-doped porous graphene	85.8 %	Molten Li infusion	23.6	LFP	0.45	87.8 % at 500 cycles
[18]	Lithiophilic carbon film	-	Molten Li infusion	22.2	Mg/Ti doped LiNiO ₂	1.6	84.0 % at 140 cycles
[19]	Au-rGO	75 %	Electrochemically deposition	-	-	-	-
[1]	Ag-CNF	~ 78 %	Electrochemically deposition	-	-	-	-
[2]	Ag-CF	75 %	Molten Li infusion	21.4	LFP	0.8	62.7 % at 5000 cycles
[20]	Amine-CNF	-	Molten Li infusion	6.32	LiNi _{0.8} Mn _{0.1} Co _{0.1} O ₂ (NMC811)	4.2	91.0 % at 200 cycles
[21]	Polyacrylamide-GO	~ 85 %	Li foil	-	LTO	-	77.0 % at 800 cycles
[22]	Au-VGCF	~ 80 %	-	-	-	-	-
[23]	3D porous carbon	~ 60 %	Electrochemically deposition	8	NMC622	4.0	87.2 % at 100 cycles
[24]	N, S-doped porous carbon	~ 91 %	Electrochemically deposition	2	LFP	2.0	-
[25]	Li/carbon cloth	-	Li foil	9.1	LTO	1.96	80.7 % at 700 cycles
[26]	3D carbon skeleton	75 %	Electrochemically deposition	10	LiNi _{0.8} Co _{0.15} Al _{0.05} O ₂	0.65	82.5 % at 200 cycles
[27]	Carbon microtube	~ 95 %	Electrochemically deposition	10	NMC532	0.75	~75.0 % at 100 cycles
[28]	3D-HCFs	~ 91 %	Electrochemically deposition	6	LFP	2.0	94.4 % at 150 cycles
[29]	PI-ZnO	-	Molten Li infusion	10	LTO	3.0	~85.0 % at 100 cycles
[30]	Carbon nanomembrane	-	Li foil	-	LFP	0.35	~69.0 % at 230 cycles
[31]	Graphitized carbon fiber	~ 88 %	Electrochemically deposition	8	LFP	2.0	80.0 % at 300 cycles
-	This work	98 %	Electrochemically deposition	2	NMC811	3.2 – 4.0	87.2 % at 500 cycles

Table S4. Summary of electrochemical performances for recently published carbon-based Li hosts.

	Before TM hydroxide coating	After TM hydroxide coating	Yield (%)
Ni hydroxide coated CC	0.2409 g	0.2529 g	104.99 %
Fe hydroxide coated CC	0.2364 g	0.2477 g	104.81 %

Table S5. Weight change of the carbon after TM hydroxide coating. The width and length of carbon cloth are 4 cm and 5 cm, respectively.

	Before the catalytic hydrogenolysis	After the catalytic hydrogenolysis	Yield (%)
hy-C	0.2529 g	0.1799 g	71.13 %
CM-hy-C	0.2477 g	0.1937 g	78.19 %

Table S6. Weight change of the carbon after TM-catalyzed hydrogenolysis. The width and length of carbon cloth are 4 cm and 5 cm, respectively.

	Before the galvanic replacement	After the galvanic replacement	Yield (%)
GR hy-C	0.1799 g	0.1791 g	99.59 %
GR CM-hy-C	0.1937 g	0.1913 g	98.75 %

Table S7. Weight change of the carbon after galvanic replacement reaction with HAuCl_4 solution. The width and length of carbon cloth are 4 and 5 cm, respectively.

Note S1 In case of the catalytic hydrogenolysis of graphite, the nickel particles in contact with edges or steps in the graphite preferentially initiate to penetrate the graphite and cut channels because atomic hydrogen is highly reactive to the edge and step sites of graphite. On this account, the channeling reaction of Ni catalyst occurs anisotropically along with the crystallographic directions of graphite. In general, the nickel catalyst can cut channels in either $\langle 11\bar{2}0 \rangle$ or $\langle 10\bar{1}0 \rangle$ direction, while the facets at the catalyst-graphite interface are always oriented parallel to the $\langle 11\bar{2}0 \rangle$ directions^{32,33}. For this reason, the channels produced by the catalytic hydrogenolysis are usually straight with occasional 60° or 120° changes in its orientation.

Note S2 It is widely studied that Au has a great lithiophilicity with essentially zero-overpotential owing to its multiple Li_xAu alloy phases and solubility into Li^{7, 34}. Despite its good lithiophilic characteristic, the use of Au as a lithiophilic seed is highly limited because Au is one of the most precise noble metals. During the galvanic replacement, TM in each sample can act as an electron sacrificial seed for reducing Au ion by dissolving itself into the solution, and Au would be normally deposited on the sacrificial TM. The galvanic replacement on pristine CC was shown in Fig.S14. Interestingly, in both galvanic replaced CM-hy-C (GR|CM-hy-C) and galvanic replaced hy-C (GR|hy-C), the Au dots were deposited not on the TM particle, but on the carbon substrate. Because the carbon substrate in these samples has a good electrical conductivity, the electrons from TM can be released and move through the carbon substrate to a region where the catalytic hydrogenolysis arose (Fig.S16). This pathway change of galvanic replacement was reported in previous studies³⁵.

We found that the Au nano-dots are placed on the surface of graphitic shell as well as the inner room of the nano-channels in CM-hy-C owing to the defective structure of graphitic shell (Fig. 2m and Fig.S17). The vacancy defects in the graphitic shell not only lowers the activation energy for Au nucleation but also accelerates the nucleation of smaller sized Au cluster. This uniform distribution of Au nano-dots would be able to effectively reduce the overpotential for Li deposition and induce a dense Li plating without the dendrite, even with infinitesimal Au content. On the contrary, the GR|hy-C, having no vacancy defects, shows exceedingly inhomogeneous Au distribution on the surface with highly uneven and larger diameter of Au dots (Fig.2n and Fig.S18). Owing to this inhomogeneous Au distribution, the GR|hy-C exhibits a severe deviation on Au content in each fiber (Fig.S18). Such large deviation on Au distribution tend to cause a fatal biased lithium deposition particularly on the Au dots.

Note S3 GR|CM-hy-C and GR|hy-C exhibited significantly low overpotential of 12 mV and 16 mV, respectively. Their low overpotentials are originated from both the enhanced chemical reactivity of carbon by the catalytic hydrogenolysis and galvanic replacement of lithiophilic Au particles whereas Cu foil displayed the highest overpotential owing to its lithiophobic characteristic. Pristine CC also showed a relatively high overpotential. The GR|CM-hy-C retained the mitigated Li nucleation overpotential with small hysteresis at various current densities up to 10 mA cm⁻² (Fig.S19 and S20).

Note S4 Although GR|hy-C had a similar Li nucleation overpotential with that of GR|CM-hy-C, it exhibited poor cycle behavior with continuous increase in the overpotential (Fig.S21). As described in Fig.1, carbon gasification is dominant in Ni-catalyzed reaction because of unstable and weak Ni–C bonding. However, in Fe-catalyzed reaction, the growth of graphitic shell by carbon supersaturation as well as the gasification occurs, and the obtained shells involve numerous vacancy defects in their graphitic structure. Additionally, these defects can act as a nucleation site for Au replacement by lowering activation energy, leading to uniform nucleation of Au nano-dots (< 10 nm) on the surface of CM-hy-C ⁷. On the other hand, Au replacement on hy-C results in sub-micron Au dots with highly localized distribution on the surface. These disparities in structural property and Au distribution between CM-hy-C and hy-C contribute to poor electrochemical performances of GR|hy-C. Electrochemical performances of CM-hy-C and hy-C before the galvanic replacement were described in Fig.S22. The voltage profile of hy-C has shown sharper voltage change than those of CM-hy-C for repeated Li plating/stripping test. This characteristic voltage change is originated from the formation of mossy-like lithium dendrite which brings about SEI fracture, randomly Li growth on the dendrite, and non-uniform Li deposition³⁶. The voltage decay associated with dramatic increase in surface area and faster electrochemical reaction by newly exposed Li surface from the formation of mossy-like lithium dendrite.

Note S5 We have performed XPS and XRD analysis for Li deposited GR|CM–hy–C to observe a phase transition mechanism of Au nano-dots along with Li deposition (Fig. S29 and S30). Before Li deposition, the pristine GR|CM–hy–C showed two distinct peaks in Au 4f of XPS spectrum which indicates metallic Au (Fig.S29). However, after 0.5 and 3.0 mAh cm⁻² of Li deposition, the peaks in Au 4f spectrum disappeared. XPS analysis is a surface analysis technique from the surface to a depth of approximately 5 nm. It implies that the Au nano-dots are covered by Li with over 5 nm thick. Notably, when considering the wide measured area of XPS analysis (over 200 μm), the absence of Au peaks indicates that all Au nano-dots in GR|CM–hy–C are uniformly covered by Li deposition even after small amount of Li plating (0.5 mAh cm⁻²). In addition, we conducted XRD measurement to investigate the phase transition of Au during Li plating process (Fig.S30). For the GR|CM–hy–C, characteristic peaks in XRD were observed only for carbon and Fe oxide, and no peak was detected for Au. This is because there is a trace amount of Au nano-dot in GR|CM–hy–C (< 0.05 wt%). After 0.5 mAh cm⁻² of Li plating, the peak for LiC₆ was observed in GR|CM–hy–C. To confirm the phase transition of Au, we prepared a GR|CM–hy–C having excessive amount of Au by the galvanic replacement reaction using 10 times higher concentrated 50 mL of 0.1 mM HAuCl₄·3H₂O solution compared with the solution used in this manuscript. This GR|CM–hy–C with excessive Au showed small peak for metallic Au in XRD analysis. After 0.5 mAh cm⁻² of Li plating, the Au peak disappeared, and peaks at 23.3 and 24.5 degree appeared indicating Li₁₅Au₄ phase. It implies that Li was plated on Au initially by alloying reaction. Based on these XPS and XRD results, it can be concluded that, during Li plating reaction, Li first forms a Li₁₅Au₄ phase by alloying reaction and being preferentially deposited on the lithiophilic Li₁₅Au₄ phase uniformly. The preferential and uniform Li deposition on Au nano-dots was observed in the SEM image of GR|CM–hy–C with 0.5 mAh cm⁻² of Li plating in Figure S28.

Note S6 In this Li-free full-cell test, GR|CM-hy-C provided a good cycle stability for 120 cycles despite its Li-free environment (Fig.S32a). Also noteworthy, there was a relatively rapid capacity drop within early 50 cycles with low Coulombic efficiency below 99.7 %. However, after 50 cycles, both the reversible capacity and cycle efficiency have stabilized over 120 cycles. Such capacity drop in early cycles would be derived from the side reactions on GR|CM-hy-C. For the GR|hy-C, it also showed rapid capacity drop in early stage similar with that of GR|CM-hy-C. However, contrary to stabilized cycle life of GR|CM-hy-C, the cycling capacity of GR|hy-C was gradually decreased even after the early rapid capacity drop. It means that GR|hy-C has relatively poor Li reversibility causing gradual loss of Li inventory for repeated cycles while GR|CM-hy-C achieves good reversibility with minimized active Li loss by its lithiophilic surface region including nano-channels and defective graphene shells. Through this Li-free full-cell test, we confirmed that the GR|CM-hy-C has about 1.0 mAh cm⁻² of capacity loss in early cycles and then it is stabilized. This lithium loss can be simply addressed by various pre-lithiation methods which have been extensively studied in both academia and industry recently. The schematic chart explaining the amount of active lithium inventory without or with the pre-lithiation is shown in Fig.S32b. The voltage profiles of the Li-free full cell and typical Li foil || NCM811 are described in Fig.S33. According to Fig.S33a and b, the Li-free GR|CM-hy-C has slightly lower discharge voltage plateau because of a capacity contribution of the carbon substrate of GR|CM-hy-C. Because the capacity contribution of the carbon cloth is small, its impact on the overall electrochemical performance is minimal.

Note S7 We have prepared the control sample using same method with preparation of Fe hydroxide coated carbon cloth described in Methods. To avoid the catalytic hydrogenolysis reaction, we applied one step annealing (500 °C for 30 min) process under Ar/H₂ (90/10 volume ratio) atmosphere with a flow rate of 0.8 L min⁻¹. The as-received carbon was coated by nano-sized Fe particles on its surface (Fig. S39), and there was no trace of the catalytic hydrogenolysis reaction. Then, we conducted a galvanic displacement reaction for the as-received carbon using 50 mL of 10 mM HAuCl₄·3H₂O which is the same solution used in the manuscript. Unlike GR|CM-hy-C having uniform distribution of Au nano-dot (Fig. S17), the galvanic replaced; Fe coated carbon cloth (GR|C) showed non-uniform Au particle distribution (Fig. S40). Furthermore, these Au particles have around 300 nm of diameter, which is about 30 times larger than that of GR|CM-hy-C. These large; unevenly distributed Au particles are incurred by absence of the defects which can act as active sites for a galvanic displacement reaction. It can lead to highly localized Li plating around the particle, resulting in dendritic Li formation.

In Li plating/stripping test, the GR|C provided a plausible performance under low current density of 0.5 mA cm⁻² because of lithiophilic Au particles on its surface (Fig. S41). However, when higher current densities (1.0 and 2.0 mA cm⁻²) were applied, the GR|C started to exhibit a severe overpotential. It is because a relatively non-uniform Li ion flux by higher current density accelerates a localized Li plating and dendritic Li formation. In full-cell test, the cell using GR|C provided a good cycle stability at the early stage, but after around 45 cycles, its cycle stability is rapidly deteriorated (Fig. S42). It has quite similar trend with the cycle degradation of GR|hy-C although the GR|hy-C has shown much better cycling performance than GR|C (Fig.4a). We also carried out SEM analysis of GR|C after Li deposition (Fig. S43 and S44). After 0.5 mAh cm⁻² of Li deposition, though the amount of deposited Li was relatively small, there were Li dendrites and localized Li deposition on the surface of GR|C (Fig. S43). In addition, after 1.5 mAh cm⁻² of Li plating, Li was mainly deposited on the top side of electrode instead of the surface of carbon fiber, in dendritic and porous form (Fig. S44). This non-uniform Li deposition behavior of GR|C is also similar with that of GR|hy-C (Fig.3k) although GR|hy-C has relatively dense Li plating owing to numerous nano-channels on its surface. Their non-uniform Li deposition would be derived from their highly localized distribution of sub-micron Au dots resulting in excessive Li plating on the specific region. Through these results, we can identify not only the effect of catalytic hydrogenolysis by comparing GR|C and GR|CM-hy-C, but the effect of nano-channels by comparing GR|C and GR|hy-C. As shown in Figure S40 and Figure S18, GR|C and GR|hy-C both have locally distributed large Au dots on their surface. On this account, they have exhibited similar trends in full-cell degradation and Li deposition behavior. However, due to numerous nano-channels on the surface of GR|hy-C, the GR|hy-C can provide better performances overall than those of GR|C.

Note S8 At the 1st cycle, it has almost zero voltage hysteresis (0.3 mV) between Li plating and stripping (Fig.S45b). As cycling progressed, its voltage hysteresis is slightly increased to 0.4 mV, 2.1 mV, and 4.3 mV, respectively (Fig.S45c-e). Similarly, NCM811 cathode maintained almost same voltage range from 4.30 V to 2.80 V even after long-term cycling around 1400 hours (Fig.S45b-e). These good cycling performances and stable voltage behavior can be attributed to the excellent lithiophilicity and Li reversibility of GR|CM-hy-C during Li plating/stripping process owing to its unique structural features.

Note S9 We have carried out additional electrochemical evaluations including rate performance, high temperature cycle stability, and direct current internal resistance (DCIR) measurement in Figure S46-S48. For the rate test, we fabricated the full-cell pairing with the GR|CM-hy-C and pristine Li foil as anode electrode. Both GR|CM-hy-C and pristine Li foil cells provided almost similar rate capability at various discharging current densities (Figure S46). It means that our GR|CM-hy-C can provide a good electrical conductivity during cell operating despite its porous structure and lean Li inventory compared with pristine Li foil. We also conducted a high temperature (60 °C) cycling test to verify thermal stabilities of each sample (Figure S47). In this cycling test, the GR|CM-hy-C showed a stable cycle life over 50 cycles while GR|C suffered a sudden drop just after 20th cycle. This poor cycle stability of GR|C would be derived from severe dendritic Li plating and poor Li reversibility by cell operating at the ambient temperature. Pristine Li foil||NCM811 exhibited a cycle stability with slightly rapid slope of capacity drop than that of GR|CM-hy-C. Additionally, we measured the DCIR for each sample to compare our sample with commercial graphite cell (Figure S48). The detailed testing protocol of DCIR was described in Method. The DCIR of GR|CM-hy-C was quite lower while the GR|C exhibited a high cell resistance because of its locally concentrated Li deposition and dendritic Li plating. The DCIR value of GR|CM-hy-C is quite competitive with that of commercial graphite cell despite its porous carbon electrode structure.

Note S10 The porous Li host having MIEC characteristic is substantially beneficial for reversible Li plating/stripping in ASSB configuration because of its balanced ion and electron transport properties³⁷⁻⁴³. Owing to these features, the porous MIEC hosts have significantly improved the reversibility of Li plating/stripping and electrochemical performance of ASSB.

Ju Li and co-workers recently published a pioneering study that clearly elucidates a mechanistic understanding of how Li migrates through porous MIEC interlayer using a simple carbon tubules structure⁴³. Their study has demonstrated the dominant Li transport pathway in which Li_{BCC} with a low melting point (~ 453 K) can propagate and retract within the 3D porous MIEC interlayer via the interfacial diffusion. In terms of kinetics, it has been suggested that the low melting point of Li_{BCC} and large interfacial area provided by the porous MIEC interlayer would allow Li atoms to diffuse rapidly along the wall or surface of the MIEC structure.

This result implies that, as lithium diffuses along the surface of the MIEC interlayer, lithium can effectively pass through the MIEC interlayer and migrate towards the anode side.

Based on these facts, lithium can migrate through our GR|CM-hy-C interlayer via the interfacial diffusion described above because the GR|CM-hy-C interlayer used in this study also has MIEC characteristics. According to the cross-sectional SEM images (Fig.5f-h), the ASSB adopting pristine Li foil as anode exhibited a porous Li plating/stripping layer derived from non-uniform Li ion flux. This inhomogeneous Li nucleation and growth can accelerate the dendritic formation of Li plating as well as side reactions by the electrolyte decomposition. On the contrary, even after 70 cycles, the GR|CM-hy-C MIEC interlayered Li foil provided a highly dense Li layer beneath the interlayer with clearly separation between the solid-state electrolyte and Li layer (Fig.5i-k and Fig.S5X). It is noticeable that the GR|CM-hy-C MIEC interlayer has become dense by filling with metallic Li into the layer during repeated cycles, compared with its surface before cycling. This morphological change in surface indicates that the Li diffuses from the solid-state electrolyte to the anode side through the surface of GR|CM-hy-C interlayer via the interfacial diffusion mechanism.

Supplemental references

1. Yang, C., Yao, Y., He, S., Xie, H., Hitz, E., and Hu, L. (2017). Ultrafine Silver Nanoparticles for Seeded Lithium Deposition toward Stable Lithium Metal Anode. *Adv. Mater.* 29, 1702714-n/a, 1702714. 10.1002/adma.201702714.
2. Zhang, R., Chen, X., Shen, X., Zhang, X.-Q., Chen, X.-R., Cheng, X.-B., Yan, C., Zhao, C.-Z., and Zhang, Q. (2018). Coralloid Carbon Fiber-Based Composite Lithium Anode for Robust Lithium Metal Batteries. *Joule* 2, 764-777. 10.1016/j.joule.2018.02.001.
3. Sun, Q., Zhai, W., Hou, G., Feng, J., Zhang, L., Si, P., Guo, S., and Ci, L. (2018). In Situ Synthesis of a Lithiophilic Ag-Nanoparticles-Decorated 3D Porous Carbon Framework toward Dendrite-Free Lithium Metal Anodes. *ACS Sustainable Chemistry & Engineering* 6, 15219-15227. 10.1021/acssuschemeng.8b03708.
4. Jin, S., Ye, Y., Niu, Y., Xu, Y., Jin, H., Wang, J., Sun, Z., Cao, A., Wu, X., Luo, Y., et al. (2020). Solid-Solution-Based Metal Alloy Phase for Highly Reversible Lithium Metal Anode. *J. Am. Chem. Soc.* 142, 8818-8826. 10.1021/jacs.0c01811.
5. Lee, Y.-G., Fujiki, S., Jung, C., Suzuki, N., Yashiro, N., Omoda, R., Ko, D.-S., Shiratsuchi, T., Sugimoto, T., Ryu, S., et al. (2020). High-energy long-cycling all-solid-state lithium metal batteries enabled by silver-carbon composite anodes. *Nat. Energy*. 10.1038/s41560-020-0575-z.
6. Lee, S., Lee, K.-s., Kim, S., Yoon, K., Han, S., Lee, M.H., Ko, Y., Noh, J.H., Kim, W., and Kang, K. (2022). Design of a lithiophilic and electron-blocking interlayer for dendrite-free lithium-metal solid-state batteries. *Science Advances* 8, eabq0153. 10.1126/sciadv.abq0153.
7. Yan, K., Lu, Z., Lee, H.-W., Xiong, F., Hsu, P.-C., Li, Y., Zhao, J., Chu, S., and Cui, Y. (2016). Selective deposition and stable encapsulation of lithium through heterogeneous seeded growth. *Nat. Energy* 1, 16010. 10.1038/nenergy.2016.10
8. Xiang, J., Yuan, L., Shen, Y., Cheng, Z., Yuan, K., Guo, Z., Zhang, Y., Chen, X., and Huang, Y. (2018). Improved Rechargeability of Lithium Metal Anode via Controlling Lithium-Ion Flux. *Adv. Energy Mater.* 0, 1802352. 10.1002/aenm.201802352.
9. Diao, W.-Y., Xie, D., Li, Y.-F., Jiang, R., Tao, F.-Y., Sun, H.-Z., Wu, X.-L., Zhang, X.-Y., and Zhang, J.-P. (2021). Sustainable and Robust Graphene Cellulose Paper Decorated with Lithiophilic Au Nanoparticles to Enable Dendrite-free and High-Power Lithium Metal Anode. *Chemistry – A European Journal* 27, 8168-8177. <https://doi.org/10.1002/chem.202100440>.
10. Yan, J., Ye, M., Zhang, Y., Tang, Y., Liu, X., and Li, C.C. (2022). Graphene-Enabled Electric-Field Regulation and Ionic Redistribution Around Lithiophilic Aurum Nanoparticles Toward a Dendrite-Free and 2000-Cycle-Life Lithium Metal Battery. *Chemistry – A European Journal* 28, e202201151. <https://doi.org/10.1002/chem.202201151>.
11. Kang, D.W., Park, S.S., Choi, H.J., Park, J.-H., Lee, J.H., Lee, S.-M., Choi, J.-H., Moon, J., and Kim, B.G. (2022). One-Dimensional Porous Li-Confinable Hosts for High-Rate and Stable Li-Metal Batteries. *ACS Nano* 16, 11892-11901. 10.1021/acsnano.2c01309.
12. C. Jin, O. Sheng, J. Luo, H. Yuan, C. Fang, W. Zhang, H. Huang, Y. Gan, Y. Xia, C. Liang, J. Zhang and X. Tao, *Nano Energy*, 2017, **37**, 177-186.
13. T.-T. Zuo, Y.-X. Yin, S.-H. Wang, P.-F. Wang, X. Yang, J. Liu, C.-P. Yang and Y.-G. Guo, *Nano Letters*, 2018, **18**, 297-301.
14. P. Shi, T. Li, R. Zhang, X. Shen, X.-B. Cheng, R. Xu, J.-Q. Huang, X.-R. Chen, H. Liu and Q. Zhang, *Advanced Materials*, 2019, **31**, 1807131.
15. S. Liu, X. Xia, Y. Zhong, S. Deng, Z. Yao, L. Zhang, X.-B. Cheng, X. Wang, Q. Zhang and J. Tu, *Advanced Energy Materials*, 2018, **8**, 1702322.
16. M. Zhu, B. Li, S. Li, Z. Du, Y. Gong and S. Yang, *Advanced Energy Materials*, 2018, **8**, 1703505.
17. G. Huang, J. Han, F. Zhang, Z. Wang, H. Kashani, K. Watanabe and M. Chen, *Advanced Materials*, 2019, **31**, 1805334.
18. L. Tao, A. Hu, Z. Yang, Z. Xu, C. E. Wall, A. R. Esker, Z. Zheng and F. Lin, *Advanced Functional Materials*, 2020, **30**, 2000585.

19. J. Pu, J. Li, Z. Shen, C. Zhong, J. Liu, H. Ma, J. Zhu, H. Zhang and P. V. Braun, *Advanced Functional Materials*, 2018, **28**, 1804133.
20. C. Niu, H. Pan, W. Xu, J. Xiao, J.-G. Zhang, L. Luo, C. Wang, D. Mei, J. Meng, X. Wang, Z. Liu, L. Mai and J. Liu, *Nature Nanotechnology*, 2019, **14**, 594-601.
21. C. Li, S. Liu, C. Shi, G. Liang, Z. Lu, R. Fu and D. Wu, *Nature Communications*, 2019, **10**, 1363.
22. Y. Yang, J. Xiong, J. Zeng, J. Huang and J. Zhao, *Chemical Communications*, 2018, **54**, 1178-1181.
23. H.-J. Noh, M.-H. Lee, B. G. Kim, J.-H. Park, S.-M. Lee and J.-H. Choi, *ACS Applied Materials & Interfaces*, 2021, **13**, 55227-55234.
24. B. Li, W. Cao, S. Wang, Z. Cao, Y. Shi, J. Niu and F. Wang, *Advanced Science*, 2022, **9**, 2204232.
25. Y. Zhou, Y. Han, H. Zhang, D. Sui, Z. Sun, P. Xiao, X. Wang, Y. Ma and Y. Chen, *Energy Storage Materials*, 2018, **14**, 222-229.
26. X. Zhou, W. Huang, C. Shi, K. Wang, R. Zhang, J. Guo, Y. Wen, S. Zhang, Q. Wang, L. Huang, J. Li, X. Zhou and S. Sun, *ACS Applied Materials & Interfaces*, 2018, **10**, 35296-35305.
27. C. Sun, T. Wu, J. Wang, W. Li, J. Jin, J. Yang and Z. Wen, *Journal of Materials Chemistry A*, 2018, **6**, 19159-19166.
28. L. Liu, Y.-X. Yin, J.-Y. Li, N.-W. Li, X.-X. Zeng, H. Ye, Y.-G. Guo and L.-J. Wan, *Joule*, 2017, **1**, 563-575.
29. Y. Liu, D. Lin, Z. Liang, J. Zhao, K. Yan and Y. Cui, *Nature Communications*, 2016, **7**, 10992.
30. S. Rajendran, Z. Tang, A. George, A. Cannon, C. Neumann, A. Sawas, E. Ryan, A. Turchanin and L. M. R. Arava, *Advanced Energy Materials*, 2021, **11**, 2100666.
31. J. Cui, S. Yao, M. Ihsan-Ul-Haq, J. Wu and J.-K. Kim, *Advanced Energy Materials*, 2019, **9**, 1802777.
32. Baker RTK, Chludzinski JJ, Sherwood RD. A comparison of the catalytic influence of nickel, iron and nickel-iron on the gasification of graphite in various gaseous environments. *Carbon* 1985, **23**(3): 245-254.
33. Schäffel F, Warner JH, Bachmatiuk A, Rellinghaus B, Büchner B, Schultz L, *et al.* Shedding light on the crystallographic etching of multi-layer graphene at the atomic scale. *Nano Research* 2009, **2**(9): 695-705.
34. Pu J, Li J, Zhang K, Zhang T, Li C, Ma H, *et al.* Conductivity and lithophilicity gradients guide lithium deposition to mitigate short circuits. *Nat Commun* 2019, **10**(1): 1896.
35. Chang C-J, Liu C-A, Pu Y-H, Yang T-Y, Chiu H-T, Chen C-H, *et al.* Gold Nanoparticles Grown by Galvanic Replacement on Graphene-Coated Aluminum Panels as Large-Area Substrates for Surface-Enhanced Raman Scattering. *ACS Applied Nano Materials* 2020, **3**(6): 5783-5793.
36. Wood KN, Noked M, Dasgupta NP. Lithium Metal Anodes: Toward an Improved Understanding of Coupled Morphological, Electrochemical, and Mechanical Behavior. *ACS Energy Letters* 2017, **2**(3): 664-672.
37. Y.-G. Lee, S. Fujiki, C. Jung, N. Suzuki, N. Yashiro, R. Omoda, D.-S. Ko, T. Shiratsuchi, T. Sugimoto, S. Ryu, J. H. Ku, T. Watanabe, Y. Park, Y. Aihara, D. Im and I. T. Han, *Nature Energy*, 2020, **5**, 299-308
38. Z. Zhu, L.-L. Lu, Y. Yin, J. Shao, B. Shen and H.-B. Yao, *ACS Applied Materials & Interfaces*, 2019, **11**, 16578-16585.
39. W. Guo, S. Liu, X. Guan, X. Zhang, X. Liu and J. Luo, *Advanced Energy Materials*, 2019, **9**, 1900193.
40. J. Yan, J. Yu and B. Ding, *Advanced Materials*, 2018, **30**, 1705105.
41. S. Y. Kim and J. Li, *Energy Material Advances*, 2021, 2021.
42. D. Spencer-Jolly, V. Agarwal, C. Doerrler, B. Hu, S. Zhang, D. L. R. Melvin, H. Gao, X. Gao, P. Adamson, O. V. Magdysyuk, P. S. Grant, R. A. House and P. G. Bruce, *Joule*, 2023, DOI: 10.1016/j.joule.2023.02.001.
43. Y. Chen, Z. Wang, X. Li, X. Yao, C. Wang, Y. Li, W. Xue, D. Yu, S. Y. Kim, F. Yang, A. Kushima, G. Zhang, H. Huang, N. Wu, Y.-W. Mai, J. B. Goodenough and J. Li, *Nature*, 2020, **578**, 251-255.